Nature Communications

https://doi.org/10.1038/s41467-026-69535-5

Article in Press

The clinical missense variant E282K in PPP3CA/calcineurin shifts substrate dephosphorylation by altering active site recruitment

Received: 5 June 2025

Accepted: 4 February 2026

Cite this article as: Shirakawa, K.T., Parikh, T., Machado, L.E. *et al.* The clinical missense variant E282K in PPP3CA/calcineurin shifts substrate dephosphorylation by altering active site recruitment. *Nat Commun* (2026). https://doi.org/10.1038/s41467-026-69535-5

Karina T. Shirakawa, Tvesha Parikh, Luciana E.S.F. Machado, Galini Poimenidou, Hieu T. Nguyen, Mark L. Dell'Acqua, Arminja N. Kettenbach, Rebecca Page & Wolfgang Peti

The clinical missense variant E282K in PPP3CA/calcineurin shifts substrate dephosphorylation by altering active site recruitment

Karina T. Shirakawa[1,2,#], Tvesha Parikh[1,#], Luciana E.S.F. Machado[3], Galini Poimenidou[4], Hieu T. Nguyen[4], Mark L. Dell'Acqua[5], Arminja N. Kettenbach[4,6], Rebecca Page[2], Wolfgang Peti[1,*]

[1]Department of Molecular Biology and Biophysics, University of Connecticut Health Center, Farmington, CT 06030, USA; [2]Department of Cell Biology, University of Connecticut Health Center, Farmington, CT 06030, USA; [3]Institute of Chemistry, University of Campinas, Campinas, SP, 13083-970, Brazil; [4]Department of Biochemistry and Cell Biology, Geisel School of Medicine at Dartmouth, Hanover, NH 03755, USA; [5]Department of Pharmacology, University of Colorado School of Medicine, Aurora, CO USA 80045, USA; [6]Dartmouth Cancer Center, Lebanon, NH 03756, USA.

[#]contributed equally

Corresponding author: Wolfgang Peti; email: peti@uchc.edu

Abstract

Recently, de novo heterozygous variants of Calcineurin (CN) were reported as the cause of a neurodevelopmental disorder that presents with epileptic encephalopathy and dysmorphism (DEE91), with the largest group of patients harboring the CN missense mutation E282K (glutamate → lysine). Here, we use molecular and cellular techniques to define how this mutation alters CN activity. We discover that basophilic substrates use an arginine residue to bind to CN via an acidic substrate recruitment pocket adjacent to the CN active site, the E282 pocket. Furthermore, we show that basic residues in the i-1 position of the substrate relative to the substrate phosphosite enhance CN-mediated dephosphorylation. While the CN_{E282K} structure shows that the overall conformation is unchanged, the E282 pocket transforms from acidic to basic, with pocket access blocked by the formation of a E282K-E237 salt bridge. Finally, in vitro assays and in cell phosphoproteomics show that CN_{E282K} shifts CN substrate dephosphorylation profiles from basic to acidic, thereby altering CN-mediated dephosphorylation signaling. Together, these data define the molecular impact of the CN_{E282K} variant in cells and development, providing a key step for developing strategies to treat this disorder and its accompanying complications.

Introduction

Phosphorylation is one of the most ubiquitous, reversible posttranslational modifications (PTM) in cells.[1] Thus, defining the finely tuned specific and reciprocal relationship between kinases and phosphatases is essential for understanding their control and modulation of signaling pathways. Calcineurin (CN, Protein Phosphatase 2B [PP2B], PP3)[2–4] is a ubiquitously expressed phosphoprotein phosphatase (PPP) that is especially abundant in the brain. Upon activation by Ca^{2+} (hence *calcineurin*),[5] CN dephosphorylates an estimated 100s-1000s of substrates to regulate development, synaptic plasticity, learning and memory as well as many other functions.[3,6,7] As a consequence, disruption of CN-regulated signaling in the brain has, for decades, been associated with disease, including Alzheimer's (AD)[8] and Parkinson's disease[9]. Large-scale whole exome sequencing (WES) has greatly advanced the identification of genetic variants that underlie disease, especially rare diseases. During the last decade, WES studies have identified multiple de novo variants of CN (*PPP3CA*) that are associated with a distinct neurodevelopmental disorder that presents with epileptic encephalopathy, intellectual disabilities, dysmorphism, hypotonia and autism spectrum disorder (PPP3CA-related DEE91 [developmental and epileptic encephalopathy]; OMIM #617711),[10–14] with the missense mutation E282K being the most frequently observed variant. Critically, the molecular mechanisms by which th*ese* de novo CN variants, including E282K, disrupt CN-mediated signaling are major open questions.

CN is a constitutive heterodimer with two subunits (Fig. 1a).[5,15] The catalytic subunit A (CNA) contains the active site, the calmodulin binding region and an auto-inhibitory domain (AID). The regulatory subunit B (CNB) binds four Ca^{2+} ions, making CN responsive to calcium signaling. Substrates and regulators are recruited to CN via CN-specific short linear motifs (SLiMs), short conserved sequences that are present within intrinsically disordered regions (IDRs) of proteins that mediate protein:protein interactions.[16–24] The PxIxIT SLiM binds the CNA subunit[16,20,21,23,24] while the LxVP SLiM binds the interface between the CNA and Ca^{2+}-sensing CNB domain;[21] the latter is accessible only upon Ca^{2+}-activation.[18,25,26] CN substrates, such as the NFATs,[17,18,22]

NHE1,[20,27] RCAN1,[23] among others, use both PxIxIT and LxVP motifs to bind CN in a 1-to-1 manner. Mutating these SLiMs in substrates abolishes dephosphorylation by CN, demonstrating the essential role of recruitment for substrate dephosphorylation.[18–21] As a consequence, simply blocking substrate recruitment is sufficient to inhibit CN-mediated dephosphorylation in cells, a mechanism exploited by viruses (i.e., A238L of the African swine fever virus) and immunosuppressants such as FK506.[21,28,29]

Recent work has shown that the efficacy of CN catalysis can be modulated by additional mechanisms. For example, a recently discovered CN active site recognition sequence (TxxP) enhances recruitment to the active site, accelerating CN-mediated dephosphorylation.[20] However, many CN substrates do not have a phosphosite TxxP sequence, suggesting there may be additional mechanisms for enhancing phosphosite dephosphorylation. One such possibility is the enhanced binding of kinase-specific phosphosite sequences that are targeted by CN for dephosphorylation. For example, CN counteracts the activities of basophilic kinases, especially PKA, which requires an R-R-x-S/T motif for productive phosphorylation.[30] How and if this basophilic kinase motif is locally recruited to the CN active site for dephosphorylation processing remains an open question.

By leveraging two model PKA/CN substrate pairs, here we show an additional recruitment pocket adjacent to the CN active site that is critical for CN substrate recruitment, specificity and regulation. The two substrates include the canonical PKA regulatory subunit II (RII)[31] that via a phosphorylation switch, controls PKA activity proceeding cAMP-binding, and the transforming growth factor beta (TGFβ) activated kinase (MAP Kinase Kinase Kinase 7 or Transforming growth factor β-activated kinase 1; TAK1)[32]. Leveraging both an in vitro peptide and cell-based proteomics approach, we tested how this pocket globally affects local CN active site recruitment. Our comprehensive structural, biochemical and proteomics data reveals that an arginine residue at the i-1 position relative to the phosphosite in CN substrates is critical for enhanced recruitment and dephosphorylation of these substrates. This enabled us to define an additional CN substrate

recruitment pocket that facilitates recruitment of basophilic substrates. Furthermore, we show that this CN substrate recruitment pocket includes the major clinical CN variant residue E282, highlighting that the E282K variant likely results in a global shift of signaling outcomes resulting in neurodevelopment deficits. Defining how CN recruits and especially dephosphorylates distinct CN-specific substrates will not only advance our understanding of the role of PPPs in modulating signaling pathways, but also provide the data needed to understand how the de novo CN variants alter this signaling and, in turn, lead to the development of routes for treating PPP3CA-related DEE91.

Results

TAK1 uses an LxVP SLiM and a RRRS motif to bind CN

TAK1 is a mitogen activated protein kinase (MAPK) that contains an N-terminal kinase domain (Fig. 1a; aa 1-306) and a C-terminal IDR (Fig. 1a; aa 306-606) that is phosphorylated by PKA at Ser439 (^{436}RRR<u>S</u>^{439}). CN counteracts the activities of many basophilic kinases, including PKA, and its sequence contains a putative LxVP motif (^{422}LDVP^{425}) near the PKA phosphorylation site.[22] Therefore we tested if the TAK1 IDR binds CN using isothermal titration calorimetry (ITC). The data showed that both the extended C-terminal IDR ($TAK1_{306-590}$) and a shorter version including the target phosphorylation site ($TAK1_{384-474}$; hereafter, TAK1) bind CN and do so with nearly identical affinities (Fig. 1b, Supplementary Figs. 1a,b; Supplementary Table 1). Consistent with these data the 2D [^{1}H,^{15}N] heteronuclear single quantum coherence (HSQC) spectra of $TAK1_{306-590}$ and TAK1 show a nearly perfect overlap of all H^N/N cross-peaks, confirming there were no local or long-range changes between the ensemble of conformations adopted in both TAK1 constructs (Supplementary Fig. 1c). We did not test if CN binds to the TAK1 catalytic domain (likely not as no CN SLiM was identified) nor if the TAK1 catalytic domain makes an intramolecular interaction with the TAK1 C-terminal IDR.

To identify the TAK1 residues that bind CN, we completed the sequence specific backbone assignment of TAK1 (Supplementary Fig. 2a) and overlaid the 2D [^{1}H,^{15}N] HSQC spectra of ^{15}N-labeled TAK1 in the absence and presence of CN (Fig. 1c,d). Many H^{N}/N cross-peaks were significantly broadened with CN (Figs. 1d,e; Supplementary Figs. 2b-e), with most reduced intensities corresponding to TAK1 residues 415-441 (Fig. 1e; includes the putative LxVP motif and residues surrounding the Ser439 PKA phosphosite). We confirmed the importance of the LxVP motif for CN recruitment using ITC, as a variant lacking the LxVP sequence ($LxVP_{dead}$: ^{422}LDVP^{425} → ^{422}AAAA^{425}) failed to bind CN (Fig. 1f).

TAK1 bound CN with an atypically strong affinity compared to other $LxVP_{peptide}$:CN interactions (TAK1 K_D, 860 ± 23 nM; Fig. 1b; other reported LxVP K_D's, ~1800-500000 nM; Supplementary Table 1),[21,23,33] suggesting that residues outside the LxVP motif contribute to CN binding. Consistent with this, in the presence of CN, the peak intensities of the consensus site for PKA phosphorylation (^{436}RRR<u>S</u>^{439}) were reduced to the same extent as those observed for the LxVP residues (Fig. 1e). To test if these residues facilitate CN binding, we mutated the PKA phosphorylation consensus sequence in TAK1 (RRR_{dead}: ^{436}RRR<u>S</u>^{439} → ^{436}AAA<u>S</u>^{439}; Fig. 1a) and measured its affinity for CN. The affinity decreased ~4.5-fold (Fig. 1g, Supplementary Table 1), demonstrating that ^{436}RRR^{438} enhances CN binding. Together, these data show that TAK1 strictly requires a functional LxVP motif to bind CN and that this is strengthened by the RRRS phosphosite motif.

The RRRS phosphosite motif binds CN near the active site

To define how the RRRS motif binds CN, we determined the crystal structure of a substrate-trapped CN complex. Trapping was achieved by using a catalytically inactive CN variant (D90A; lacks the M1 active site metal and thus is unable to dephosphorylate substrates) and a thiophosphorylated TAK1 substrate (*tp*, thiophosphorylated; hereafter, CN_{D90A}:tpTAK1, Figs. 2a,b; tethered to the PxIxIT site using CN-specific the A238L viral inhibitor peptide, Supplementary

Figs. 3a,b, Supplementary Table 2). Two copies of the CN_{D90A}:tpTAK1 complex were present in the asymmetric unit, with clear electron density for TAK1 residues bound to the CN LxVP binding pocket and the CN active site (Figs. 2b-d; Supplementary Figs. 3c-g; aa 422-428, 435-442; no density was observed for aa 429-434, which form a dynamic linker between the LxVP binding pocket and CN active site). The TAK1 LxVP motif (^{422}LDVP^{425}) binds the CN LxVP binding pocket in a manner identical to those observed previously (Fig. 2c). TAK1 Leu422 and Val424 bind two deep hydrophobic pockets at the CNA/B interface. Electron density was also observed at the CN active site, corresponding to TAK1 residues ^{436}RRR*tp*S^{439} (Figs. 2c,d). While the conformations of the Leu422 and Val424 sidechains were nearly identical between the two copies of TAK1 in the asymmetric unit, as is typical for buried hydrophobic interactions, the arginine side chains of the RRRS motif (^{436}RRR^{438}) adopted slightly different conformations between the two copies, highlighting that these charge:charge interactions are more dynamic (i.e., fuzzy; Supplementary Figs. 3c-g). TAK1 arginine residues bind an extended acidic pocket on CN (Fig. 2d), making polar and/or ionic interactions (<4 Å) with CN residues Glu282 and Gln284 (100% conserved in CN from yeast to humans; Figs. 2e, Supplementary Fig. 3h). Arg438 (R_{i-1} relative to *tp*S), which is immediately adjacent to the active site, makes the most extensive interactions with CN, binding a deep, strongly acidic pocket defined by Glu237 and Glu282 (Fig. 2e).

Arginine i-1 phosphosite recruitment facilitates efficient TAK1 dephosphorylation

To quantify the contribution of these CN residues for TAK1 binding, we performed ITC measurements of TAK1 vs CN_{E282K}, CN_{Q284K} and CN_{D285K}. The data showed that affinity of TAK1 for CN_{E282K} is 3-fold weaker than CN_{WT} (akin to TAK1 RRR_{dead}; Supplementary Fig. 4a, Supplementary Table 1), while binding is only minimally impacted for TAK1 vs CN_{Q284K} or CN_{D285K} (Supplementary Figs. 4b,c Supplementary Table 1). These data highlight the key role of the R_{i-1} residue for binding. Next, we performed CN dephosphorylation assays. We mutated these residues in the CN substrate binding pocket and measured their ability to dephosphorylate TAK1

*p*Ser439 (uniformly PKA-phosphorylated Ser439, *p*S439, was achieved using the $TAK1_{S389A/S417A}$ variant, as NMR experiments showed that in vitro Ser389 and Ser417 are partially, non-specifically phosphorylated by PKA). The data showed that CN variants with mutations in residues near the i-2 and i-3 arginine residues (Q284K, D285K, Y315A), had an increase in activity (Fig. 2f). In contrast, mutating the residues that define the CN i-1 pocket—E237K and E282K—significantly reduced activity, by ~50% and ~70%, respectively (Fig. 2f, Table 1). To further confirm that the arginine in the i-1 position facilitates TAK1 binding at the active site, we generated the TAK1 R438V variant (^{436}RR<u>R</u>S^{439} → ^{436}RR<u>V</u>S^{439}) and measured its affinity for CN and CN_{E282K} using ITC (Supplementary Fig. 4d, Supplementary Table 1). The data showed that the lack of an arginine in the i-1 position weakens the affinity ~3-fold, nearly to the same extent observed for the TAK1 RRR_{dead} variant, but, as reasoned, has very minimal effect on CN_{E282K} binding (Supplementary Fig. 4e, Supplementary Table 1). Together, these data identify a negatively charged pocket, the E282 pocket, that facilitates the recruitment and dephosphorylation of substrates containing an arginine residue in the i-1 position (R_{i-1}).

Arginine in the i-1 position is a general mechanism for enhanced CN substrate dephosphorylation

We next tested the generality of an arginine in the i-1 position for enhancing CN-mediated recruitment and dephosphorylation of CN substrates by measuring the dephosphorylation of a canonical CN substrate that lacks an i-1 arginine: the PKA regulatory subunit RII (RII Ser99 is phosphorylated and dephosphorylated by PKA and CN, respectively, and lacks an i-1 arginine, ^{96}RRVS^{99}; RII_{44-103} construct used for these studies; hereafter RII). We also created an RII variant where the i-1 residue was mutated to arginine (Fig. 3a; i.e., contains an R_{i-1}). Like TAK1, RII also uses an LxVP motif for CN recruitment, which we confirmed using NMR spectroscopy and X-ray crystallography (Fig. 2c, Supplementary Figs. 5a-d, Supplementary Table 2). To assay CN-mediated dephosphorylation, we phosphorylated Ser99 in wt RII and the R_{i-1} RII variant (RII_{V98R}; ^{96}RR<u>V</u>S^{99} → ^{96}RR<u>R</u>S^{99}) using PKA (phosphorylation assays performed using the $RII_{S58A/S78A}$

construct to ensure phosphorylation of only Ser99). The data showed that replacing Val98 with an arginine in the RII i-1 position enhanced CN-mediated dephosphorylation by ~50% compared to WT, confirming the enhanced dephosphorylation of substrates with an arginine in the i-1 position (Fig. 3b; Table 2). Second, while the i-1 pocket charge reversal variants CN_{E237K} and CN_{E282K} reduced the dephosphorylation of wt RII, the decrease in activity was significantly more pronounced with the RII_{V98R} variant, by ~70% and ~85%, respectively (Fig. 3b; Table 2). Together, these data confirm the role of the acidic binding pocket adjacent to the CN active site, the E282 binding pocket, for CN substrate recruitment of CN R_{i-1} containing substrates.

CN_{E282K} fails to effectively recruit R_{i-1}-dependent CN substrates

These results show that the CN E282 binding pocket has a critical role in recruiting R_{i-1}-containing substrates to the CN active site to facilitate their dephosphorylation. The most frequently observed variant in PPP3CA-related DEE91 is E282K (Fig. 4a). To test if the altered dephosphorylation of R_{i-1}-containing substrates in CN_{E282K} is due to a global or local change in CN conformation, we determined the crystal structure of CN_{E282K} (Fig. 4b; bound to NHE1, a peptide that binds CN using a PxIxIT and LxVP motif[20]; Fig. 2c). The structures of CN_{WT} and CN_{E282K} (both bound to NHE1) are nearly identical (RMSD, 0.16 Å; Figs. 4b,c), demonstrating that there are no global changes in the CN_{E282K} conformation. The conformation of bound NHE1 is also identical, confirming that the CN_{E282K} PxIxIT and LxVP recruitment pockets are fully structured and functional (Fig. 4b); i.e., they are not impacted by the E282K mutation. The most significant change is observed in the E282 pocket itself, where E282K forms a salt bridge with E237, which likely sterically hinders substrate access to the E282 pocket (Fig. 4c). Furthermore, an analysis of the electrostatic surface potential of CN_{E282K} shows that the negative charge of the R_{i-1} binding pocket is significantly attenuated compared to the substrate-trapped complex (Figs. 4d-f).

To test if these changes impact TAK1 binding at the E282 binding pocket, we repeated the NMR analysis of TAK1 with CN_{E282K} (Supplementary Figs. 6a-f). As expected, an overlay of

the 2D [^{1}H,^{15}N] HSQC spectrum of ^{15}N-labeled TAK1$_{384-474}$ in the absence and presence of CN$_{E282K}$ showed that many H^{N}/N cross-peaks were significantly broadened partially beyond detection upon complex formation; however, the broadening observed for the TAK1 RRRS motif was less than that observed with CN$_{WT}$, demonstrating that CN$_{E282K}$ recruits R$_{i-1}$ containing substrates less effectively, consistent with their lower K$_{D}$s in ITC measurements and their inability to be efficiently dephosphorylated (Supplementary Fig. 6e,f). These data suggest that the observed changes in substrate recruitment and dephosphorylation by CN$_{E282K}$ are due to local changes at the E282 binding pocket.

To further confirm our findings, we generated additional TAK1 variants and compared their dephosphorylation efficiency with CN vs CN$_{E282K}$. As expected, TAK1 R438K (^{436}RR<u>R</u>S^{439} → ^{436}RR<u>K</u>S^{439}) showed no differences, while reversing the charge by creating an TAK1 R438D or R438E variant (^{436}RR<u>R</u>S^{439} → ^{436}RR<u>D</u>S^{439} or ^{436}RR<u>R</u>S^{439} → ^{436}RR<u>E</u>S^{439}) showed, as expected, increased dephosphorylation by CN$_{E282K}$ when compared to wt-TAK1 (Fig. 4g). We also tested the effect of deleting the i-2 or i-3 arginine side chains. TAK1 R436A (^{436}RRRS^{439} → ^{436}<u>A</u>RRS^{439}) showed an additional small decrease in activity (highlighting that the ensemble of structures is less influenced by the likely interactions between the positive charged arginine and the negative charged phosphor moiety), while TAK1 R437A (^{436}RRRS^{439} → ^{436}R<u>A</u>RS^{439}) showed a small increase in dephosphorylation. Lastly, we also tested the TAK1 R438V (^{436}RR<u>R</u>S^{439} → ^{436}RR<u>V</u>S^{439}) and showed that its activity is slightly increased for CN$_{E282K}$. Thus, both local electrostatic and substrate accessibility changes at the E282 pocket in the CN$_{E282K}$ variant result in the weakened recruitment and dephosphorylation of R$_{i-1}$-containing substrates, and, therefore, is likely the molecular basis of the altered signaling that gives rise to PPP3CA-related DEE91.

The PPP3CA-related DEE91 CN missense mutation E282K globally alters CN substrate dephosphorylation

To determine the general importance of CN E282 for substrate recruitment and dephosphorylation, we performed an in vitro phosphoproteomics assay. Here, we quantified the differences between CN_{WT}- and CN_{E282K}-mediated dephosphorylation of substrates derived from a HeLa cell phosphopeptide library. Asynchronous HeLa cells were treated with the pan-PPP inhibitor Calyculin A for 30 minutes to induce a hyperphosphorylated state. Proteins extracted from these cells were digested with Lys-C to preserve arginine residues that are part of dephosphorylation motifs surrounding the phosphosites. These peptides were incubated with CN_{WT} and CN_{E282K} in vitro for 0, 15, 30, 60 and 120 minutes to determine CN sequence preferences in a time-dependent manner (Fig. 5a, Supplementary Fig. 7a; Supplementary Data 1). This resulted in 1274 substrate peptides for CN_{WT} and 1267 substrate peptides for CN_{E282K}, respectively. Using hierarchical clustering, we identified four clusters with fast, intermediate, or slow dephosphorylation kinetics or sites that were not dephosphorylated (Supplementary Fig. 7b). Next, we extracted peptides with either arginine (R), lysine (K), aspartate (D) or glutamate (E) amino acids in the i-1 position and compared their dephosphorylation rates (Fig. 5b). The data show that CN_{WT} readily dephosphorylates peptides with R-pS/T and K-pS/T motifs, while CN_{E282K} dephosphorylates these peptides more slowly (Fig. 5c). Conversely, CN_{E282K} dephosphorylates peptides with D/E-pS/T motifs faster than CN_{WT} (Fig. 5c). These data confirm the importance of the negatively charged E282 active site recruitment pocket for CN activity and, furthermore, highlights how a single point variant, CN_{E282K}, globally alters the CN substrate recruitment and dephosphorylation (Fig. 5c, Supplementary Fig. 7b). We also determined the amino acid enrichment of all phosphorylation sites in the fast dephosphorylation cluster of CN_{WT} and CN_{E282K}, which confirmed the preference of CN_{WT} for basic and CN_{E282K} for acidic residues in the i-1 position (Fig. 5d).[34]

CN_{E282K} substrate preference in cells

To determine if CN_{WT} and CN_{E282K} display differential substrate preferences in cells, we stably expressed them in HEK293T cells and performed MS-IP and quantitative phosphoproteomics (Supplementary Figs. 8a,b). The MS-IP CN_{WT} vs control data identified many established CN interactors, including NFATs, RCANs, constituents of the PI4K complex,[35] NUP proteins,[36] GSK3 kinases, SIK kinases and RANB3, all of which have been previously identified in CN MS data.[33,36] Comparing the MS-IP data between CN_{WT} vs CN_{E282K} showed that RCAN2/3 are enriched in CN_{E282K} vs CN_{WT} (as RCAN1 has been shown to bind at the CN active site,[23] it is possible that a similar active site interaction in RCAN2/3 may influence CN binding). Interestingly, most other known interactors showed depletion with CN_{E282K}, including PI4K.[35,37] Next, we analyzed the HEK293T-based quantitative phosphoproteomics data. Here, we compared sequences surrounding single, localized phosphosites dephosphorylated by CN_{WT} or CN_{E282K} (Supplementary Figs. 8c,d, Supplementary Data 2). Consistently, as in our in vitro results, we observed an enrichment of arginines and lysines in the -1 position for CN_{WT} and glutamate and aspartate for CN_{E282K}.

To determine if the HEK293T MS data is mirrored in a cell line more physiologically relevant for DEE91, we repeated the MS-IP and quantitative phosphoproteomics measurements of CN_{WT} and CN_{E282K} in N2A cells, a neuronal mouse neuroblastoma cell line that has been widely used to study neuronal functions and disorders. The MS-IP CN_{WT} vs control data identified again many established CN interactors, confirming our ability to perform these experiments in N2A cells and highlighting the consistency between the HEK293T and N2A CN interactomes (Fig. 6a). We then assessed if known CN interactors exhibit altered recruitment with CN_{E282K}. While the RCANs and NFATC3 were enriched with CN_{E282K}, many interactors were depleted, including the PI4K complex (Fig. 6b). Thus, the N2A MS-IP data largely mirrored that from HEK293T cells. We then analyzed the N2A-based quantitative phosphoproteomics data (Fig. 6c), which, like the HEK293T data, showed an enrichment of positively charged residues in the -1 position for CN_{WT} and glutamate for CN_{E282K} (Fig. 6d; Supplementary Data 2). We also analyzed which proteins

experienced the largest increase or decrease in (de)phosphorylation, which, surprisingly, included many proteins not previously shown to be regulated or modulated, directly or indirectly, by CN (Fig. 6c). Because direct substrates of CN are recruited via CN-specific SLiMs, we used a bioinformatics pipeline to identify if CN-specific SLiMs (PxIxIT and LxVP) are present in these potential CN substrates (Supplementary Figs. 9a,b). The data show that all but one of the putative substrates contain 1 or more PxIxIT, LxVP or both SLiMs, highlighting the most differently affected phosphosites in N2A cells are putative direct CN substrates.

Together, our comprehensive in vitro and cellular data confirm that, as observed for TAK1 and RII, CN has a preference at the active site for substrates with an arginine residue the i-1 position relative to the phosphosite in CN substrates. This residue is recruited by a negatively charged pocket consisting of E282 and E237. Together, with the previously defined TxxP motif, our data shows the importance of active site interactions for CN dephosphorylation and how a single residue substitution, E282K, can shift the overall substrate preference of CN.

Discussion

Recruiting substrates with high fidelity is essential for signaling enzymes, such as PPPs. Because PPPs are metalloenzymes, with the necessary residues that coordinate metal binding being 100% conserved between the family members, this enzyme family, unlike many kinase families, mostly lacks specificity at the active site.[38,39] Instead, PPPs use protein:protein interactions, often mediated by PPP-specific SLiMs, to maintain PPP-to-substrate fidelity.[20,21,24] While the ubiquitous PPP CN shares many common PPP family traits, including SLiM-based recruitment of regulators and substrates,[21,22,24,33] its active site is unusual compared to other family members. For example, the most common pan-PPP inhibitors, such as microcystin-LR or nodularin, only weakly inhibit CN, highlighting that its active site geometry differs from that of other PPPs.[40] Moreover, it was recently reported that CN does exhibit specificity near its active site, preferentially recruiting substrates containing an S/TxxP motif.[23] Here, we expand on this CN distinctiveness by

identifying a second active site recruitment motif that facilitates CN-mediated dephosphorylation of substrates. Our data show that a negatively charged pocket adjacent to the CN active site, the E282 pocket, enhances the recruitment of CN substrates with an R_{i-1} residue, which in turn facilitates the placement of the *p*S/T phosphosite at the active site. This suggests that the E282 pocket is particularly important for counteracting basophilic kinase phosphosites in CN substrates, such as PKA sites. Indeed, while the active site recruitment sequence of PKA is defined as RRxS,[30] the dephosphorylation counterpart CN leverages an xxRS motif. This CN active site recruitment is sufficiently enhanced so that it enabled the structure of CN bound to a PKA phosphorylated substrate to be determined. The structure, coupled with structure-based functional assays, defined the importance of the E282 pocket for basophilic substrate binding. It also showed that this recruitment pocket is mediated largely by charge:charge interactions (often referred to as a fuzzy interaction),[41] allowing for increased dynamics, and thus may provide energetic advantages for the local substrate binding interaction. Indeed, by creating a peptide library from PPP-inhibited HeLa cells and HEK293T cells expressing CN_{WT} and CN_{E282K}, we showed that this active site recruitment is necessary for a broad range of peptide sequences. These findings are important as they will allow for the much faster identification of additional CN substrates.

This discovery is particular important as various genetic studies have identified dozens of clinical CN variants that cause severe neurodevelopmental disease in children and young adults, characterized by seizures, chronic pain, global developmental delays, autism and epilepsy, now collectively referred to as PPP3CA-related DEE91.[10–14,42] Some of these CN variants involve active site residues, that either limit CN activity by preventing metals from binding at the active site (which is necessary for activity) or destabilizing substrate engagement at the active site. However, the mechanism by which other variants alter CN activity and function is unknown. While the number of reported patients is still small, the CN_{E282K} is the most frequently identified variant. As we show here, E282 defines the R_{i-1} binding pocket. Its mutation to a lysine reverses its charge

from acidic to basic and weakens not only the recruitment and dephosphorylation of basophilic substrates like TAK1 but, as we show, globally alters substrate preference from basophilic to acidophilic both in vitro and in cells. These results not only provide a molecular basis for altered signaling in patients with the E282K variant but will enable future detailed CN proteomics studies to understand the consequences on specific CN substrates. Fortunately, scores of cell biological and biochemical studies have advanced our understanding of CN substrates,[19,20,22,33,43] allowing for a detailed analysis that will eventually define the CN substrates that are most affected by the E282K mutation and, in turn, allow for a comprehensive understanding of the alterations in signaling events. Taken together, our data highlights that CN functions differently than the rest of the PPPs by leveraging active site recruitment sites. This data will help to further our understanding of CN substrates and most importantly has set the stage to develop routes to overcome the devastating developmental effects clinical CN variants have.

Methods

Cloning. $TAK1_{384-474}$/$TAK1_{384-474}$ $LxVP_{dead}$ (AAAA)/$TAK1_{384-474}$ RRR_{dead} (AAAS) were subcloned into pTHMT containing an N-terminal His_6-MBP for enhanced solubility followed by tobacco etch virus (TEV) protease cleavage site tag. Additionally, $TAK1_{306-590}$ and $TAK1_{384-474}$ were subcloned into pRP1b containing an N-terminal His_6-tag followed by a TEV protease cleavage site. A $TAK1_{384-474}$ variant (S389A, S417A; S389 and S417 are non-specifically phosphorylated by PKA as detected by NMR spectroscopy) was created by site-directed mutagenesis and exclusively used for CN dephosphorylation assays. Site-directed mutagenesis was performed in $TAK1_{384-474}$ (S389A, S417A) to generate R436A (^{436}ARR^{438}), R437A (^{436}RAR^{438}), R438K (^{436}RRK^{438}), R438V (^{436}RRV^{438}), R438E (^{436}RRE^{438}) and R438D (^{436}RRD^{438}) variants.

RII_{44-103} was subcloned into pTHMT and site-directed mutagenesis was performed to generate RII_{44-103} (S58A, S78A; S58 and S78 are non-specifically phosphorylated by PKA as detected by NMR spectroscopy) and RII_{44-103}V98R (S58A, S78A) for dephosphorylation assays. CN_{391} (CNA; 1-391, CNB; 1-169) was subcloned into pRP1b as a single bicistronic cassette containing an N-terminal His_6-tag followed by a TEV protease cleavage site. CN_{391} variants; E237K, E282K, Q284K, D285K, and Y315A variants (CNA subunit variants) were generated by site-directed mutagenesis from CN_{391} wildtype construct. The A238L-TAK1 peptide was designed as a G-Block containing residues of the African Swine Viral protein A238L PxIxIT motif (PKIIIT) and linker (aa 200-228) and the LxVP motif and RRRS motif from TAK1 (aa 422-440) (TAK1 chimera, motifs underlined: GHMRRFKKK<u>PKIIIT</u>GCEDNVYEKLPEQNSNF^{422}<u>LDVP</u>EIVISGNGQP<u>RRRS</u>I^{440}RP, RP was added to the C-terminus to enhance the binding to the active site and facilitate crystallization). The A238L-TAK1 peptide sequence was subcloned into the pRP1b vector containing a His_6-tag followed by a TEV protease cleavage site. The $NHE1_{679-723}$ peptide was subcloned into the pTHMT vector and used for CN_{E282K} crystallization studies. For crystallization experiments, CNA_{1-370} (hereafter, CNA_{370}), CNB_{1-170} or CNB_{15-170} were subcloned into pCDF_Duet1 (CNA in MCS1 and CNB in MCS2). CNA contains an N-terminal His_6-tag followed

by a TEV protease cleavage site. Site-directed mutagenesis was performed on CNA_{370} to generate the D90A and E282K variants. All variants were sequence verified.

Protein Expression. TAK1 (WT and variants), *RII* (WT and variants) and the *A238L-TAK1* chimera proteins were expressed in *Escherichia coli* BL21 (DE3) cells (Agilent). CN_{391} plasmids (WT and variants) were transformed into *E. coli* BL21 (DE3) RIL cells (Agilent). Freshly transformed cells were grown at 37 °C in LB medium containing appropriate antibiotics (kanamycin [50 μg mL^{-1}] for TAK1, RII and A238L-TAK1 plasmids; kanamycin [50 μg mL^{-1}] and chloramphenicol [34 μg mL^{-1}] for CN_{391} plasmids) until they reached an optical density (OD_{600}) of ~0.8. Protein expression was induced by addition of 1 mM isopropyl β-d-thiogalactopyranoside (IPTG) to the growth and incubated for 18 h at 18 °C, 250 rpm. Cells were harvested by centrifugation (6,000 *x* g, 20 min, 4°C) and stored at -80°C until purification. For NMR experiments, expression of uniformly ^{13}C- and/or ^{15}N-labeled protein was carried out by growing freshly transformed cells in M9 minimal media containing 4 g L^{-1} [^{13}C]-D-glucose and/or 1 g L^{-1} $^{15}NH_4Cl$ (Cambridge Isotopes Laboratories) as the sole carbon and nitrogen sources, respectively.

$NHE1_{679-723}$ was expressed in *E. coli* BL21 (DE3) RIL cells (Agilent). Freshly transformed cells were grown at 37 °C in LB medium containing the appropriate antibiotics (kanamycin [50 μg mL^{-1}] and chloramphenicol [34 μg mL^{-1}]) until an OD_{600} of ~0.8 was reached. Protein expression was induced by addition of 1 mM IPTG and cultures were allowed to grow overnight (18–20 h, 250 rpm shaking) at 18 °C. Cells were collected by centrifugation (6,000 *x* g, 15 min, 4 °C) and stored at -80 °C until purification.

CNA_{370}/CNB_{1-170} (WT) *and CNA_{370}/CNB_{15-170}* (WT, E282K, D90A) were expressed in *E. coli* BL21 (DE3) RIL cells (Agilent). Freshly transformed cells were grown at 37 °C in LB medium containing the antibiotics (spectinomycin [120 μg mL^{-1}] and chloramphenicol [34 μg mL^{-1}]) until they reached an OD_{600} of ~0.8. Protein expression was induced by addition of 1 mM IPTG to the growth and

incubated for 18 h at 18 °C, 250 rpm. Cells were harvested by centrifugation (6,000 *x* g, 20 min, 4°C) and stored at -80 °C until purification.

PKA (human Cα1 in pet15b) was transformed into *E. coli* BL21 (DE3) RIL cells (Agilent). Freshly transformed cells were grown at 37 °C in LB medium containing the appropriate antibiotics (carbenicillin [100 µg mL^{-1}] and chloramphenicol [34 µg mL^{-1}]) until an OD_{600} of ~0.8 was reached. Protein expression was induced by addition of 1 mM IPTG to the culture medium, and cultures were allowed to grow overnight (18–20 h, 250 rpm shaking) at 18 °C. Cells were collected by centrifugation (6,000 *x* g, 15 min, 4 °C) and stored at -80°C until purification.

Protein Purification. For all constructs, cell pellets were resuspended and homogenized in ice-cold lysis buffer (50 mM Tris pH 8, 500 mM NaCl, 5 mM Imidazole, 0.1% Triton-X-100) or CN lysis buffer (20 mM Tris pH 7.5, 300 mM NaCl, 50 µM $CaCl_2$, 0.1% Triton X-100) with EDTA-free protease inhibitor tablet (ThermoFisher), lysed by high-pressure cell homogenization (Avestin Emulsiflex C3). Cell debris was pelleted by centrifugation (45,000 *x* g, 45 min, 4 °C) and the supernatant was filtered using 0.22 µm syringe filters (Millipore) before purification.

TAK1 and RII. His_6-MBP-tagged $TAK1_{384-474/306-590}$ or RII_{44-103} (S58A, S78A) (WT and variants) and His_6-tagged $TAK1_{384-474}$ (S389A, S417A) (WT and variants) was loaded onto a HisTrap HP column (Cytiva) pre-equilibrated with Buffer A (50 mM Tris pH 8.0, 500 mM NaCl, 5 mM Imidazole). Proteins were eluted using a linear gradient of 0-80% Buffer B (50 mM Tris pH 8.0, 500 mM NaCl, 500 mM Imidazole). Fractions containing the protein were pooled and dialyzed in buffer ([TAK1, 20 mM Tris pH 8.0, 500 mM NaCl], [RII, 20 mM CHES pH 9, 50 mM NaCl, 0.5 mM TCEP]) overnight at 4 °C with TEV protease (in-house, His_6-tagged) to cleave the His_6-MBP-tag or His_6-tag. Following cleavage, the sample was loaded under gravity onto Ni^{2+}-NTA beads (Prometheus) pre-equilibrated with Buffer A. Proteins were eluted using a stepwise-elution of Buffer B (5-100%). The flow-through and wash A fractions were collected and then heat purified by incubating the samples at 80 °C/TAK1 and 75 °C/RII, for 15 minutes. Samples were centrifuged at 4,000 *x* g for

15 min to remove precipitated proteins. $TAK1_{384-474}$ (S389A, S417A) was aliquoted, flash frozen and stored at -80 °C for phosphorylation reactions. $TAK1_{384-474}$ or RII_{44-103} (S58A, S78A) supernatant was concentrated and purified using size exclusion chromatography (SEC; HiLoad 26/600 Superdex 75 [Cytiva]) in TAK1 NMR Buffer (20 mM HEPES pH 6.5, 50 mM NaCl, 0.5 mM TCEP) or RII NMR buffer (20 mM HEPES pH 6.5, 50 mM NaCl, 0.5 mM TCEP) or SEC buffer, TAK1 (20 mM Tris pH 8.0, 50 mM NaCl, 0.5 mM TCEP) or RII (20 mM HEPES pH 7.0, 50 mM NaCl, 0.5 mM TCEP). Purified samples were heat purified for a second time at 80 °C for TAK1 and 75 °C for RII for 15 min and were either used directly for NMR data collection or flash frozen and stored at -80 °C for ITC (TAK1) or dephosphorylation assays (RII).

A238L-TAK1 chimera. Supernatant was loaded under gravity onto Ni^{2+}-NTA beads pre-equilibrated with Buffer A (50 mM Tris pH 8.0, 500 mM NaCl, 5 mM Imidazole) and eluted using a stepwise gradient 5-100% Buffer B (50 mM Tris pH 8.0, 500 mM NaCl, 500 mM Imidazole). Fractions containing the protein were pooled and dialyzed (20 mM Tris pH 8.0, 500 mM NaCl) overnight at 4 °C with TEV protease to cleave the His_6-tag. Following dialysis and cleavage, the dialyzed sample was loaded under gravity onto Ni^{2+}-NTA beads pre-equilibrated with Buffer A. The flow-through and wash A fractions were collected and heat purified at 70 °C for 20 min, centrifuged at 4,000 *x* g for 10 min to remove precipitation. The sample was concentrated and was either directly used or flash frozen and stored at −80 °C.

$NHE1_{679-723}$. His_6-MBP-tagged $NHE1_{679-723}$ was loaded onto a HisTrap HP column pre-equilibrated with Buffer A (50 mM Tris pH 8.0, 500 mM NaCl, 5 mM Imidazole). Proteins were eluted using a linear gradient of 0-80% Buffer B (50 mM Tris pH 8.0, 500 mM NaCl, 500 mM Imidazole). Fractions containing the protein were pooled and dialyzed (50 mM Tris pH 7.5, 500 mM NaCl, 0.5 mM TCEP) overnight at 4 °C with TEV protease to cleave the His_6-MBP tag. Following cleavage, the sample was loaded under gravity onto Ni^{2+}-NTA beads pre-equilibrated with Buffer A. The flow-through and wash A fractions were collected and then heat purified by incubating the samples at 75 °C for 15 min. Samples were centrifuged at 4,000 *x* g for 15 minutes to remove

precipitated proteins. $NHE1_{679-723}$ supernatant was concentrated and purified using SEC (HiLoad 26/600 Superdex 75) in CN SEC Buffer (20 mM Tris pH 7.5, 100 mM NaCl, 1 mM $CaCl_2$, 0.5 mM TCEP). Purified samples were a second time heat purified at 75 °C for 15 min and was either used directly for co-purification with CN or flash frozen and stored at -80 °C for future purifications.

CN_{391} wildtype/variants (activity assays) and CN_{370} (crystallization with RII). Supernatant was loaded onto a HisTrap HP column pre-equilibrated with Buffer A (50 mM Tris pH 8.0, 500 mM NaCl, 5 mM Imidazole) and eluted using a linear gradient of 0-80% Buffer B (50 mM Tris pH 8.0, 500 mM NaCl, 500 mM Imidazole). Fractions containing the protein were pooled and dialyzed overnight (20 mM Tris pH 7.5, 25 mM NaCl, 1 mM $CaCl_2$, 0.5 mM TCEP) at 4 °C with TEV protease to cleave the His_6-tag. Following cleavage, the sample was loaded under gravity onto Ni^{2+}-NTA beads pre-equilibrated with low salt His Buffer A (50 mM Tris pH 8.0, 25 mM NaCl, 5 mM Imidazole) and eluted stepwise with 5-100% low salt His Buffer B (50 mM Tris pH 8.0, 25 mM NaCl, 500 mM Imidazole). Flow-through and wash A fractions were collected and loaded directly onto HiTrap Q HP column for further purification. The proteins were loaded with IEX Binding Buffer (20 mM Tris pH 8, 25 mM NaCl, 1 mM $CaCl_2$, 0.1 mM TCEP) and eluted with a linear gradient 0-80% of IEX Elution Buffer (20 mM Tris pH 8, 800 mM NaCl, 1 mM $CaCl_2$, 0.1 mM TCEP). CN fractions were pooled, concentrated and further purified via SEC (HiLoad 26/600 Superdex 75; 20 mM Tris pH 7.5, 100 mM NaCl, 1 mM $CaCl_2$, 0.5 mM TCEP). Samples were either directly used or flash frozen and stored at −80 °C.

CNA_{370}(D90A)/CNB_{15-170}:A238L-tpTAK1, CNA_{370}(E282K)/CNB_{15-170}:$NHE1_{679-723}$ co-purification (for crystallization). CN variant supernatants were loaded onto a HisTrap HP column pre-equilibrated with Buffer A (20 mM Tris pH 8, 500 mM NaCl, 5 mM Imidazole) and eluted using a linear gradient 0-80% with Buffer B (20 mM Tris pH 8, 500 mM NaCl, 500 mM Imidazole). Fractions containing CN variants were pooled; for CN_{370}(D90A) a 1.5x-excess (molar concentration) A238L-*tp*TAK1 (thiophosphorylated) was added and for CN_{370}(E282K) a 2x-excess (molar concentration) $NHE1_{679-723}$ was added. Both complexes were dialyzed (20 mM Tris pH 8.0,

25 mM NaCl, 1 mM $CaCl_2$, 0.5 mM TCEP) overnight at 4 °C with TEV protease to cleave the His_6-tag. Following dialysis and cleavage, the complex sample was loaded under gravity onto Ni^{2+}-NTA beads pre-equilibrated with Buffer A. The flow-through, and wash fractions were collected, concentrated, and centrifuged at 4,000 *x* g for 10 min to remove precipitated proteins. The supernatant containing the CN complexes were further purified using SEC (HiLoad 26/600 Superdex 75; 20 mM Tris pH 8.0, 100 mM NaCl, 1 mM $CaCl_2$, 0.5 mM TCEP). Fractions from the peak containing the complex were pooled, concentrated, and either directly used for crystallography or flash frozen and stored at -80 °C.

PKA. Supernatant was loaded onto a HisTrap HP column pre-equilibrated with Buffer A (50 mM Tris pH 8.0, 500 mM NaCl, 5 mM imidazole) and eluted using a linear gradient (0–80%) with Buffer B (50 mM Tris pH 8.0, 500 mM NaCl, 500 mM imidazole). Fractions containing the protein were pooled and dialyzed overnight into PKA buffer (20 mM Tris pH 8, 50 mM NaCl, 1 mM EDTA, 2 mM DTT) at 4 °C. Purified sample was centrifuged at 15,000 *x* g for 10 min to remove precipitated protein. Supernatant protein sample was mixed with 50% glycerol, flash frozen and stored at −80 °C.

A238L-TAK1 thiophosphorylation for crystallization. Purified A238L-TAK1 chimera peptide was incubated with PKA kinase at 10:1 ratio (peptide:kinase) in phosphorylation buffer (100 mM Tris pH 7.5, 2 mM DTT, 10 mM $MgCl_2$) with 10 µM ATP-γ-S (Sigma) for thiophosphorylation. The reaction was incubated at 37 °C for 72 h. Thio-phosphorylated A238L-TAK1 (A238L-*tp*TAK1) was heat purified at 70 °C for 30 min and centrifuged (4,000 *x* g, 10 min) to remove precipitated PKA kinase. The final sample was concentrated, aliquoted in small volumes, snap frozen and stored at -80 °C until used for crystallization.

Sequence Specific Backbone Assignment. For TAK1, all NMR measurements were collected on a Bruker Avancel 500 MHz spectrometer with a HCN TCI z-gradient cryoprobe at 283 K. The sequence specific backbone assignment was determined by collecting a suite of heteronuclear NMR spectra: 2D [^{1}H,^{15}N] HSQC, 3D HNCA, 3D HN(CO)CA, 3D HNCACB, 3D CBCA(CO)NH and 3D (H)CC(CO)NH (τ_m = 12 ms). For RII, all NMR data were collected on Bruker Advance Neo 600 MHz NMR spectrometer with HCN TCI z-gradient cryoprobe at 283 K. The sequence specific backbone assignment was determined by collecting a suite of heteronuclear NMR spectra: 2D [^{1}H,^{15}N] HSQC, 3D HNCA, 3D HN(CO)CA, 3D HNCACB, 3D CBCA(CO)NH, 3D HNCO, and 3D HN(CA)CO. Both dataset spectra were processed in Topspin (Bruker Topspin v.2.1/4.1.3/4.4) and referenced to internal DSS. Peak picking and sequence-specific assignment for TAK1 and RII were performed using the program CARA v.1.9 (http://www.cara.nmr.ch).

NMR Interaction Studies of TAK1/RII with CN_{391}(WT) *and CN_{391}*(E282K)*.* All NMR interaction data of $TAK1_{384-474}$/RII_{44-103} with either CN_{391}(WT) or CN_{391}(E282K). was recorded using either a Bruker Neo 600 MHz or 800 MHz spectrometer equipped with a HCN TCI active z-gradient cryoprobe at 283 K. All NMR measurements of all $TAK1_{384-474}$/RII_{44-103} constructs were recorded using ^{15}N-labeled protein in $TAK1_{384-474}$/RII_{44-103} NMR buffer and 90% H_2O/10% D_2O. For $TAK1_{384-474}$ interaction studies, an excess of unlabeled CN_{391}(WT) or CN_{391}(E282K) (3-fold molar excess) was added to ^{15}N-$TAK1_{384-474}$ before the 2D [^{1}H,^{15}N] HSQC spectrum was collected. For RII_{44-103} interaction studies, an excess of unlabeled CN_{391}(WT) (2-fold molar excess) was added to^{15}N-labelled RII_{44-103} before the 2D [^{1}H,^{15}N] HSQC spectrum was collected. NMR data were processed using nmrPipe[44] and the intensity data were analyzed in Poky[45] (Build: 20230213). For $TAK1_{384-474}$/$RII_{44-103,}$ the intensity data was normalized to the C-terminal residue. The difference in peak heights between the free 2D [^{1}H,^{15}N] HSQC spectrum of $TAK1_{384-474}$/RII_{44-103} was compared to its respective peak, if present, on the 2D [^{1}H,^{15}N] HSQC spectrum of $TAK1_{384-474}$/RII_{44-103} in complex with CN_{391}(WT) or CN_{391}(E282K) (Microsoft Excel, v2301, b16.0.16026.20002 and GraphPad

Prism v.10.2.2). Any overlapping peaks were omitted for analysis. Poky (Build: 20230213) was used to display spectra overlays.

CN complex crystallization.

CNA_{370}(D90A)/$CNB_{15\text{-}170}$:A238L-tpTAK1 (hereafter CN_{D90A}:tpTAK1). Crystals of the CN_{D90A}:tpTAK1 complex were grown using the vapor diffusion hanging drop method, obtained after two rounds of micro-seeding and crystallization condition optimization. Purified CN_{D90A}:tpTAK1 complex was crystallized in 0.2 M sodium sulfate decahydrate, pH 6.7, 20% (w/v) PEG 3,350 or 0.2 M sodium phosphate dibasic dihydrate, pH 9.1, 20% (w/v) PEG 3,350 at 4.5 mg/mL in drop ratios 1:1, 1:2 and 2:1 (protein:solution). Thin, long, ragged needles appeared after 5-8 days and were used to prepare seed stock A. For the initial round of micro-seeding, seed stock A was diluted at 1:20 ratio with 0.2 M sodium citrate tribasic pH 8.4, 20% (w/v) PEG 3,350, and added to CN_{D90A}:tpTAK1 at 5 mg/mL in 0.2 M sodium citrate tribasic pH 8.4, 22% (w/v) PEG 3,350, 3% (v/v) ethanol in drop ratios 5:8:1 and 5:4:1 (protein:solution:micro-seeding; 1 µL: 1.6 or 0.8 µL: 0.2 µL). Crystals appeared after 7 days and were used to prepare seed stock B. For the second round of micro-seeding, seed stock B was diluted the same way as seed stock A, and added to the CN_{D90A}:tpTAK1 complex at 6.3 mg/mL in 0.2 M sodium citrate tribasic pH 8.4, 22% (w/v) PEG 3,350, 3% (v/v) ethanol in drop ratios 5:8:1 and 5:4:1. Long, thick plates appeared after 6 days. Crystals were grown using hanging drop vapor diffusion method at room temperature (22 °C). The seed stock was prepared by mixing 10 µL of the reservoir solution in each drop five times and transferring to a 1.5 mL tube containing a seed bead (Hampton Research). The process was repeated until there was a total of 50 µL in the seed bead tube. The crystals were crushed by vortexing the tube with the bead for 1 min followed by 1 min on ice (repeated five times), and 5 µL aliquots were snap frozen and stored at -80 °C for further use. Single crystals were cryoprotected with a mix of the reservoir solution and 15% glycerol before flash cooled in liquid nitrogen for data collection.

CN:RII. CN_{370} was incubated with a 1.2-fold molar excess of RII and concentrated to 6 mg/ml. Crystals formed in 3 days in 100 mM sodium citrate, pH 5.0, 100 mM $MgCl_2$-$6H_2O$, 15% (w/v) PEG 4,000. Crystals were cryoprotected using silicon oil and flash frozen in liquid nitrogen. *CN_{E282K}:NHE1*. CNA_{370}(E282K)/CNB_{15-170}:NHE1 (hereafter CN_{E282K}:NHE1) was concentrated to 8 mg/mL. Crystallization was performed using Gryphon LCP (Art Robbins) into Intelli 3-well plates (Art Robbins). Initial crystallization trials were performed in the conditions used for crystallizing the CN:NHE1 complex, resulting in small needle clusters. Conditions optimized by testing varying high pH buffers (CHES/CAPS/TRIS/HEPES) and testing varying low MW PEGs (PEG 400 – PEG 6,000). Small, moon shaped crystals were observed in 0.1 M CAPS pH 9, 0.2 M $MgCl_2$-$6H_2O$ (v/v), 24% PEG 600. Crystals were cryo-protected with paraffin oil and flash frozen in liquid nitrogen.

Data collection, processing and structure solution and refinement. Data processing and refinement statistics for all complexes reported in Table S2 with example electron density shown in Supplementary Figs. 3, 10.

CN_{D90A}:tpTAK1 and CN_{E282K}:NHE1. X-ray diffraction data were collected at the National Synchrotron Light Source II (NSLS-II) AMX 17-ID-1 beamline at Brookhaven National Laboratory (Upton, NY, US), at 100 K and a wavelength of 0.92 Å with 0.2-degree oscillations. Raw data were integrated and scaled using autoPROC (v.1.0.5)[46] with XDS software package (Jun 2023, build 20230630),[47] POINTLESS (v.1.12.10)[48] and AIMLESS (v.0.7.7)[49]. The *CN_{D90A}:tpTAK1* structure was solved by molecular replacement (MR) using Phaser (v.2.8.3) in PHENIX (v.1.20.1-4487)[50] with the structure of CN:A238L (PDB ID: 4F0Z [https://doi.org/10.2210/pdb4F0Z/pdb][21]) as the search model. The *CN_{E282K}:NHE1* structure was solved by MR using Phaser in PHENIX with the structure of CN:NHE1 (PDB ID: 6NUC [https://doi.org/10.2210/pdb6NUC/pdb][20]) as a search model. The initial models of the complex were built using Phenix AutoBuild, followed by iterative rounds of refinement in PHENIX and manual building using Coot (v.0.9.8.7 EL).[51] The

A238L-TAK1 chimera peptide position in CN_{D90A}:tpTAK1 was verified using PHENIX Polder maps.[52]

CN:RII. X-ray diffraction data were collected using a Bruker Metal Jet liquid gallium source (wavelength of 1.34 Å) with a photon III detector and the raw data were integrated and scaled using Bruker Proteum processing software, POINTLESS (v.1.11.16) and AIMLESS (0.7.3). The CN:RII structure was solved by MR using Phaser (v.2.8.3) in PHENIX (v.1.20.1-4487)[50] with the structure of CN (PDB ID: 5SVE [https://doi.org/10.2210/pdb5SVE/pdb][22]) as the search model. The initial models of the complex were built using PHENIX AutoBuild, followed by iterative rounds of refinement in PHENIX and manual building using Coot (v.0.9.8.7 EL[51]).

ITC. ITC experiments were performed at 25°C using either a VP-ITC (Microcal), an Affinity SV ITC microcalorimeter (TA Instruments) or a Nano SV ITC microcalorimeter (TA instruments). All protein samples were dialyzed in ITC buffer (20 mM HEPES pH 7.5, 100 mM NaCl, 1 mM $CaCl_2$, 0.5 mM TCEP) prior to performing ITC. TAK1 variants were titrated into CN_{WT}, CN_{E282K}, CN_{Q284K}, or CN_{D285K} (for all ITC measurements CN_{391} was used) Titrant (10 µL per injection) was injected into the sample cell over a period of 20 seconds with a 200-300 second interval between titrations to allow for complete equilibration and baseline recovery. 25 injections were delivered during each experiment, and the solution in the sample cell was stirred at 175 rpm or 350 rpm to ensure rapid mixing. Datasets were converted using NanoAnalyze (v.3.10.0) and the converted datasets were analyzed with a one set binding site model using NITPIC (v.1.2.2[53,54]) and SedPhat (v.12.1b[55]). For each SedPhat evaluation the experimental parameters were set for the buffer used (HEPES buffer pH 7.5 at 25 °C) and the cell concentration was corrected using the correction factor and fit local to account for small concentrations errors, as the less error-prone concentration is advised to be the one fixed.[56] The outlier data points were excluded from the analysis, and analysis was carried out using the model 'A + B ↔ AB Hetero-Association' and curve-fitting with Marquardt-

Levenberg nonlinear least-squares. Graphs were plotted using GUSSI (v.1.2.1)[57] and all thermodynamic parameters reported are based on the average of three or more replicates.

Phosphorylation of substrates for dephosphorylation assays. $TAK1_{384-474}$ (S389A, S417A; S389 and S417 are non-specifically phosphorylated by PKA as detected by NMR spectroscopy) and variants were phosphorylated by PKA for 18 hrs at 37 °C at a 1:50 ratio (PKA:TAK1) in phosphorylation buffer (100 mM Tris pH 7.5, 2 mM DTT, 10 mM $MgCl_2$) and 2 mM ATP (Sigma). Phosphorylated $TAK1_{384-474}$(S389A, S417A) was heat purified at 70 °C for 15 min, and the soluble fraction was further purified using anion exchange chromatography (MonoQ 5/50 GL column [Cytiva]) column pre-equilibrated with TAK1 IEX buffer A1 ($TAK1_{wt}$: 20 mM Tris pH 8, 0.1 mM TCEP) or A2 ($TAK1_{variants}$: 20 mM HEPES pH 7, 0.1 mM TCEP) and eluted with a linear gradient of increasing concentrations of 0-80% TAK1 IEX buffer B1 ($TAK1_{wt}$: 20 mM Tris pH 8.0, 800 mM NaCl, 0.1 mM TCEP) or B2 ($TAK1_{variants}$: 20 mM HEPES pH 7, 800 mM NaCl, 0,1 mM TCEP). The fractions containing *p*$TAK1_{384-474}$ (S389A, S417A) WT and variants were pooled and dialyzed (20 mM Tris pH 8.0, 50 mM NaCl, 0.1 mM TCEP) at 4 °C for 16 h to remove trace phosphate species. The final sample was concentrated, flash frozen and stored at −80 °C to be used for dephosphorylation assays.

RII_{44-103} (S58A, S78A; S58 and S78 are non-specifically phosphorylated by PKA as detected by NMR spectroscopy) and RII_{44-103}V98R (S58A, S78A) were phosphorylated by PKA for 18 hours at 37 °C in a 1:10 ratio (PKA:RII) in phosphorylation buffer (100 mM Tris pH 7.5, 2 mM DTT, 10 mM $MgCl_2$) with 500 µM ATP (Sigma). Phosphorylated RII (pRII) was concentrated and purified using SEC (HiLoad 26/600 Superdex 75) using RII SEC buffer (20 mM HEPES pH 7.0, 50 mM NaCl, 1 mM DTT). Fractions containing pRII were further dialyzed for 16-18 h at 4 °C (20 mM HEPES pH 7.0, 50 mM NaCl, 1 mM DTT) to remove trace phosphate species. pRII was concentrated, flash frozen and stored at −80 °C to be used for dephosphorylation assays.

Dephosphorylation Assays. Assays were designed using PiColorLock 600 kit (Abcam) and performed in 96-well flat-bottom plates with low evaporation lids (Costar). Control wells were included to ensure absence of trace phosphate species, 3 negative control reactions were implemented: without enzyme/substrate, enzyme only (3 concentrations) and substrate only (blank). Buffer and enzymes were added to appropriate wells, and dephosphorylation reactions were initiated by the addition of phosphorylated substrate (pTAK1 or pRII). All reactions were carried out at 37 °C for 30 mins and quenched with GoldMix mixed with Accelerator at 1:100 ratio, incubated for 5 minutes and mixed, followed by addition of Stabilizer. Measurements were carried out on a CLARIOStar plate reader (BMG Labtech) at 635 nm. A minimum of three replicates were run for each substrate/enzyme. Data was blanked against wells containing substrate only and normalized against wildtype to calculate % activity. Graphs were plotted using GraphPad Prism (v.10.2.2).

In vitro dephosphorylation assay. Asynchronous HeLa was lysed in lysis buffer (8 M urea, 50 mM Tris pH 8.1, 150 mM NaCl, 2 mM sodium beta-glycerophosphate, 2 mM sodium fluoride, 2 mM sodium molybdate, 1 mM sodium orthovanadate, mini-Complete EDTA-free protease inhibitor cocktail tablet). Protein concentration was determined by BCA assay (Pierce/Thermo Fisher Scientific). Proteins were then reduced with 5 mM DTT at 55 °C for 30 mins, cooled to room temperature, and alkylated with 15 mM iodoacetamide at room temperature for 45 mins in the dark. Alkylation reactions were quenched with an additional 5 mM of DTT. The lysates were then diluted 6-fold with 25 mM Tris pH 8.1 before tryptic digestion with 1:100 (w/w) trypsin (Sigma) at 37 °C overnight. The next day, digests were quenched by acidification with triofluoroacetic acid (TFA), centrifuged to remove precipitation, desalted, and peptides were lyophilized.

Phosphopeptide enrichment was carried out using a High Select Fe-NTA Phosphopeptide Enrichment Kit (ThermoFischer Scientific) following the manufacturer's instruction and desalted.

All phosphopeptides were combined and split into eleven equal portions. Phosphopeptides were resuspended in 166 mM EPPS pH 8.5 and the respective TMT reagent of the TMT-11plex (ThermoFischer Scientific), followed by incubation at room temperature for 1 hour. A sample was removed to determine labeling efficiency, while the remainder was stored at -80 °C. Labeling was confirmed to be at least 95% efficient before quenching with hydroxylamine. TMT-labeled phosphopeptides were separately desalted and stored in 60% methanol at -80 °C. TMT-labeled phosphopeptides were aliquoted and speed vacuum to dryness before dephosphorylation. Phosphatases were added to in vitro phosphatase dephosphorylation buffer (50 mM Tris pH 7.5, 150 mM NaCl, 1 mM $MnCl_2$, 1 mM $MgCl_2$) before adding to dried phosphopeptides for dephosphorylation. All reactions were quenched at their respective time point with 1% TFA and stored at -20 °C. Once all reactions were completed, they were combined before desalted and analyzed by LC-MS^3. Triplicate dephosphorylation time series were performed for each phosphatase. TMT-labeled peptides were analyzed on an Orbitrap Lumos mass spectrometer (ThermoFisher Scientific) equipped with an Easy-nLC 1200 (ThermoFisher Scientific), and raw data was searched and processed as previously described.[42] All phosphopeptides detected were filtered for single phosphorylated peptides with a false localization rate <0.1%. Furthermore, only phosphopeptides that were detected and quantified in 2 out of 3 replicates were picked to proceed with further analysis. Pair-wise correlation coefficient values were calculated using the Excel formula CORREL. Subsequently, p-values were calculated using the Excel formula T.DIST.2T with t-score derived from correlation coefficient values. Duplicated quantifications with the lowest p-values were selected for further analysis. The phosphorylation ratio at each time point for each phosphopeptide was calculated by dividing the TMT quantification at that time point by the maximum TMT quantification of all time points for that peptide. Data were input into Perseus[58] (v2.0.11.0) for further analysis. Unsupervised hierarchical clustering of phosphopeptides was performed using Euclidean distance. For each phosphatase, four clusters were defined based on

their dephosphorylation kinetics, from fastest to non-regulated. For motif generation, the web based application IceLogo[34] was used.

Phosphoproteomics Analysis. Flag-tagged CN_{WT} and CN_{E282K} were stably expressed in HEK293T (ATCC CRL-3216) and N2A cells (ATCC CCL-131). After selection with G418, equal expression was confirmed by western blotting. Control, CN_{WT}, and CN_{E282K} HEK293T cells were lysed in lysis buffer, digested, phosphopeptide enriched, and TMT labeled as described above. After off-line separation,[59] peptide fractions were analyzed by LC-MS[3] and raw data were searched and processed as previously described.[42] All phosphopeptides detected were filtered for single phosphorylated peptides with a false localization rate <0.25% and data were input into Perseus[58] (v2.0.11.0) for T-test statistical analysis. For motif generation, the web based application IceLogo[34] was used.

To identify CN SLiMs sites in proteins identified in the N2A phosphoproteomics data, we used both the ScanProsite tool from the Prosite database[60]. For the search, the full-length protein sequence, and specific definitions of the PxIxIT and LxVP SLiM motifs were used. For the PxIxIT site search,[19] P-x-[FILV]-x-[FILV]-x was used as query; for the LxVP site,[33] [NQDESRTH]-[YRTDFILV]-[LIVF]-x-[VPLIHA]-x was used as query. Disorder prediction via IUPred3[61] was used to calculate the disordered score for the identified SLiMs to ensure that putative SLiM sites are in an IDR (IUPred score ≥0.4) based on a previous CN SLiM analysis.[22]

Immunoprecipitations. Flag-tagged CN_{WT} and CN_{E282K} were stably expressed in HEK293T and N2A cells. After selection with G418, equal expression was confirmed by western blotting. For immunoprecipitation, cells were lysed in lysis buffer (50 mM Tris pH 7.5, 500 mM NaCl and 0.5% (w/v) Triton X-100, with an EDTA-free protease inhibitor tablet (Roche) per 10 mL of lysis buffer). Flag-tagged proteins were purified using Flag M2 affinity gel (Sigma) rotated end over end for 3 h at 4°C. The beads were washed five times with lysis buffer and eluted with 3XFlag peptide.

Proteins were precipitated using the SP3 methods[62] and digested overnight in 50 mM ammonium bicarbonate with trypsin (Promega) for mass spectrometric analysis.

Data Availability

The NMR data generated in this study have been deposited in the BioMagResBank database under accession code BMRB 51895 [https://dx.doi.org/10.13018/BMR51895] (Sequence-specific backbone assignment of the intrinsically disordered C-terminal tail of TAK1) and 52982 [https://dx.doi.org/10.13018/BMR52982] (Sequence-specific backbone assignment of the cAMP-dependent protein kinase type II-alpha regulatory subunit disordered region (aa 44-103)). The atomic coordinates and structure factors generated in this study have been deposited in the PDB database under accession code 9NXE [https://doi.org/10.2210/pdb9NXE/pdb], 9NXF [https://doi.org/10.2210/pdb9NXF/pdb], 9NXN [https://doi.org/10.2210/pdb9NXN/pdb], 4F0Z [https://doi.org/10.2210/pdb4F0Z/pdb], 6NUC [https://doi.org/10.2210/pdb6NUC/pdb] and 5SVE [https://doi.org/10.2210/pdb5SVE/pdb]. The raw mass spectrometry data is available at ProteomeXchange PXD064473 [http://proteomecentral.proteomexchange.org/cgi/GetDataset?ID=PXD064473] and PXD070300 [http://proteomecentral.proteomexchange.org/cgi/GetDataset?ID=PXD070300] and MassIVE MSV000098060 [https://massive.ucsd.edu/ProteoSAFe/dataset.jsp?task=3714453b38b844cbbd8d5a35446320a9] and MSV000099747 [https://massive.ucsd.edu/ProteoSAFe/dataset.jsp?task=b9958cb55d234bcebf59af63e7a81442]. ITC/SPR and enzymatic data generated in this study are provided in the Supplementary Information and/or Source Data file, which is available at Figshare (https://doi.org/10.6084/m9.figshare.29250827) and as a Source Data file.

References

1. Olsen, J. V. *et al.* Quantitative phosphoproteomics reveals widespread full phosphorylation site occupancy during mitosis. *Sci. Signal.* **3**, ra3 (2010).
2. Leslie, S. N. & Nairn, A. C. cAMP regulation of protein phosphatases PP1 and PP2A in brain. *Biochim. Biophys. Acta Mol. Cell Res.* **1866**, 64–73 (2019).
3. Khan, R., Kulasiri, D. & Samarasinghe, S. Functional repertoire of protein kinases and phosphatases in synaptic plasticity and associated neurological disorders. *Neural Regen. Res.* **16**, 1150–1157 (2021).
4. Foley, K., McKee, C., Nairn, A. C. & Xia, H. Regulation of Synaptic Transmission and Plasticity by Protein Phosphatase 1. *J. Neurosci. Off. J. Soc. Neurosci.* **41**, 3040–3050 (2021).
5. Klee, C. B., Crouch, T. H. & Krinks, M. H. Calcineurin: a calcium- and calmodulin-binding protein of the nervous system. *Proc. Natl. Acad. Sci. U. S. A.* **76**, 6270–6273 (1979).
6. Rusnak, F. & Mertz, P. Calcineurin: form and function. *Physiol. Rev.* **80**, 1483–1521 (2000).
7. Saraf, J. *et al.* A Friend or Foe: Calcineurin across the Gamut of Neurological Disorders. *ACS Cent. Sci.* **4**, 805–819 (2018).
8. Braithwaite, S. P., Stock, J. B., Lombroso, P. J. & Nairn, A. C. Protein phosphatases and Alzheimer's disease. *Prog. Mol. Biol. Transl. Sci.* **106**, 343–379 (2012).
9. Silva, J. D., Jupiter, D. C. & Taglialatela, G. Reduced Prevalence of Parkinson's Disease in Patients Prescribed Calcineurin Inhibitors. *J. Park. Dis.* **14**, 533–543 (2024).
10. Myers, C. T. *et al.* De Novo Mutations in PPP3CA Cause Severe Neurodevelopmental Disease with Seizures. *Am. J. Hum. Genet.* **101**, 516–524 (2017).
11. Mizuguchi, T. *et al.* Loss-of-function and gain-of-function mutations in PPP3CA cause two distinct disorders. *Hum. Mol. Genet.* **27**, 1421–1433 (2018).
12. Panneerselvam, S. *et al.* PPP3CA truncating variants clustered in the regulatory domain cause early-onset refractory epilepsy. *Clin. Genet.* **100**, 227–233 (2021).
13. Qian, Y. *et al.* Early-onset infant epileptic encephalopathy associated with a de novo PPP3CA gene mutation. *Cold Spring Harb. Mol. Case Stud.* **4**, a002949 (2018).
14. Rydzanicz, M. *et al.* Novel calcineurin A (PPP3CA) variant associated with epilepsy, constitutive enzyme activation and downregulation of protein expression. *Eur. J. Hum. Genet. EJHG* **27**, 61–69 (2019).
15. Kissinger, C. R. *et al.* Crystal structures of human calcineurin and the human FKBP12-FK506-calcineurin complex. *Nature* **378**, 641–644 (1995).
16. Li, H., Zhang, L., Rao, A., Harrison, S. C. & Hogan, P. G. Structure of calcineurin in complex with PVIVIT peptide: portrait of a low-affinity signalling interaction. *J. Mol. Biol.* **369**, 1296–1306 (2007).
17. Aramburu, J. *et al.* Selective inhibition of NFAT activation by a peptide spanning the calcineurin targeting site of NFAT. *Mol. Cell* **1**, 627–637 (1998).
18. Rodríguez, A. *et al.* A conserved docking surface on calcineurin mediates interaction with substrates and immunosuppressants. *Mol. Cell* **33**, 616–626 (2009).
19. Wigington, C. P. *et al.* Systematic Discovery of Short Linear Motifs Decodes Calcineurin Phosphatase Signaling. *Mol. Cell* **79**, 342-358.e12 (2020).
20. Hendus-Altenburger, R. *et al.* Molecular basis for the binding and selective dephosphorylation of Na+/H+ exchanger 1 by calcineurin. *Nat. Commun.* **10**, 3489 (2019).
21. Grigoriu, S. *et al.* The molecular mechanism of substrate engagement and immunosuppressant inhibition of calcineurin. *PLoS Biol.* **11**, e1001492 (2013).
22. Sheftic, S. R., Page, R. & Peti, W. Investigating the human Calcineurin Interaction Network using the πϕLxVP SLiM. *Sci. Rep.* **6**, 38920 (2016).
23. Li, Y. *et al.* The structure of the RCAN1:CN complex explains the inhibition of and substrate recruitment by calcineurin. *Sci. Adv.* **6**, (2020).

24. Li, H. *et al.* Balanced interactions of calcineurin with AKAP79 regulate Ca2+-calcineurin-NFAT signaling. *Nat. Struct. Mol. Biol.* **19**, 337–345 (2012).
25. Park, S., Uesugi, M. & Verdine, G. L. A second calcineurin binding site on the NFAT regulatory domain. *Proc. Natl. Acad. Sci. U. S. A.* **97**, 7130–7135 (2000).
26. Nygren, P. J. & Scott, J. D. Regulation of the phosphatase PP2B by protein–protein interactions. *Biochem. Soc. Trans.* **44**, 1313–1319 (2016).
27. Hisamitsu, T., Nakamura, T. Y. & Wakabayashi, S. Na(+)/H(+) exchanger 1 directly binds to calcineurin A and activates downstream NFAT signaling, leading to cardiomyocyte hypertrophy. *Mol. Cell. Biol.* **32**, 3265–3280 (2012).
28. Griffith, J. P. *et al.* X-ray structure of calcineurin inhibited by the immunophilin-immunosuppressant FKBP12-FK506 complex. *Cell* **82**, 507–522 (1995).
29. Jin, L. & Harrison, S. C. Crystal structure of human calcineurin complexed with cyclosporin A and human cyclophilin. *Proc. Natl. Acad. Sci. U. S. A.* **99**, 13522–13526 (2002).
30. Johnson, J. L. *et al.* An atlas of substrate specificities for the human serine/threonine kinome. *Nature* **613**, 759–766 (2023).
31. Fruman, D. A., Klee, C. B., Bierer, B. E. & Burakoff, S. J. Calcineurin phosphatase activity in T lymphocytes is inhibited by FK 506 and cyclosporin A. *Proc. Natl. Acad. Sci. U. S. A.* **89**, 3686–3690 (1992).
32. Olsen, J. V. *et al.* Global, in vivo, and site-specific phosphorylation dynamics in signaling networks. *Cell* **127**, 635–648 (2006).
33. Brauer, B. L. *et al.* Leveraging New Definitions of the LxVP SLiM To Discover Novel Calcineurin Regulators and Substrates. *ACS Chem. Biol.* https://doi.org/10.1021/acschembio.9b00606 (2019) doi:10.1021/acschembio.9b00606.
34. Colaert, N., Helsens, K., Martens, L., Vandekerckhove, J. & Gevaert, K. Improved visualization of protein consensus sequences by iceLogo. *Nat. Methods* **6**, 786–787 (2009).
35. Ulengin-Talkish, I. *et al.* Palmitoylation targets the calcineurin phosphatase to the phosphatidylinositol 4-kinase complex at the plasma membrane. *Nat. Commun.* **12**, 6064 (2021).
36. Wigington, C. P. *et al.* Systematic Discovery of Short Linear Motifs Decodes Calcineurin Phosphatase Signaling. *Mol. Cell* **79**, 342-358.e12 (2020).
37. Shaw, A. L. *et al.* Structure of calcineurin bound to PI4KA reveals dual interface in both PI4KA and FAM126A. *Struct. Lond. Engl. 1993* S0969-2126(24)00324–1 (2024) doi:10.1016/j.str.2024.08.007.
38. Brautigan, D. L. & Shenolikar, S. Protein Serine/Threonine Phosphatases: Keys to Unlocking Regulators and Substrates. *Annu. Rev. Biochem.* **87**, 921–964 (2018).
39. Brautigan, D. L. Protein Ser/Thr phosphatases--the ugly ducklings of cell signalling. *FEBS J.* **280**, 324–345 (2013).
40. MacKintosh, C., Beattie, K. A., Klumpp, S., Cohen, P. & Codd, G. A. Cyanobacterial microcystin-LR is a potent and specific inhibitor of protein phosphatases 1 and 2A from both mammals and higher plants. *FEBS Lett.* **264**, 187–192 (1990).
41. Fuxreiter, M. Context-dependent, fuzzy protein interactions: Towards sequence-based insights. *Curr. Opin. Struct. Biol.* **87**, 102834 (2024).
42. Papke, C. M. *et al.* A disorder-related variant (E420K) of a PP2A-regulatory subunit (PPP2R5D) causes constitutively active AKT-mTOR signaling and uncoordinated cell growth. *J. Biol. Chem.* **296**, 100313 (2021).
43. Ulengin-Talkish, I. & Cyert, M. S. A cellular atlas of calcineurin signaling. *Biochim. Biophys. Acta Mol. Cell Res.* **1870**, 119366 (2023).
44. Delaglio, F. *et al.* NMRPipe: A multidimensional spectral processing system based on UNIX pipes. *J. Biomol. NMR* **6**, 277–293 (1995).
45. Lee, W., Rahimi, M., Lee, Y. & Chiu, A. POKY: a software suite for multidimensional NMR and 3D structure calculation of biomolecules. *Bioinforma. Oxf. Engl.* **37**, 3041–3042 (2021).

46. Vonrhein, C. *et al.* Data processing and analysis with the autoPROC toolbox. *Acta Crystallogr. D Biol. Crystallogr.* **67**, 293–302 (2011).
47. Kabsch, W. XDS. *Acta Crystallogr. D Biol. Crystallogr.* **66**, 125–132 (2010).
48. Evans, P. Scaling and assessment of data quality. *Acta Crystallogr. D Biol. Crystallogr.* **62**, 72–82 (2006).
49. Evans, P. R. & Murshudov, G. N. How good are my data and what is the resolution? *Acta Crystallogr. D Biol. Crystallogr.* **69**, 1204–1214 (2013).
50. Liebschner, D. *et al.* Macromolecular structure determination using X-rays, neutrons and electrons: recent developments in Phenix. *Acta Crystallogr. Sect. Struct. Biol.* **75**, 861–877 (2019).
51. Emsley, P., Lohkamp, B., Scott, W. G. & Cowtan, K. Features and development of Coot. *Acta Crystallogr. D Biol. Crystallogr.* **66**, 486–501 (2010).
52. Liebschner, D. *et al.* Polder maps: improving OMIT maps by excluding bulk solvent. *Acta Crystallogr. Sect. Struct. Biol.* **73**, 148–157 (2017).
53. Keller, S. *et al.* High-precision isothermal titration calorimetry with automated peak-shape analysis. *Anal. Chem.* **84**, 5066–5073 (2012).
54. Scheuermann, T. H. & Brautigam, C. A. High-precision, automated integration of multiple isothermal titration calorimetric thermograms: new features of NITPIC. *Methods San Diego Calif* **76**, 87–98 (2015).
55. Zhao, H., Piszczek, G. & Schuck, P. SEDPHAT – A platform for global ITC analysis and global multi-method analysis of molecular interactions. *Methods* **76**, 137–148 (2015).
56. Brautigam, C. A., Zhao, H., Vargas, C., Keller, S. & Schuck, P. Integration and global analysis of isothermal titration calorimetry data for studying macromolecular interactions. *Nat. Protoc.* **11**, 882–894 (2016).
57. Brautigam, C. A. Chapter Five - Calculations and Publication-Quality Illustrations for Analytical Ultracentrifugation Data. in *Methods in Enzymology* (ed. Cole, J. L.) vol. 562 109–133 (Academic Press, 2015).
58. Tyanova, S. *et al.* The Perseus computational platform for comprehensive analysis of (prote)omics data. *Nat. Methods* **13**, 731–740 (2016).
59. Grassetti, A. V., Hards, R. & Gerber, S. A. Offline pentafluorophenyl (PFP)-RP prefractionation as an alternative to high-pH RP for comprehensive LC-MS/MS proteomics and phosphoproteomics. *Anal. Bioanal. Chem.* **409**, 4615–4625 (2017).
60. Sigrist, C. J. A. *et al.* New and continuing developments at PROSITE. *Nucleic Acids Res.* **41**, D344-347 (2013).
61. Erdős, G., Pajkos, M. & Dosztányi, Z. IUPred3: prediction of protein disorder enhanced with unambiguous experimental annotation and visualization of evolutionary conservation. *Nucleic Acids Res.* **49**, W297–W303 (2021).
62. Hughes, C. S. *et al.* Single-pot, solid-phase-enhanced sample preparation for proteomics experiments. *Nat. Protoc.* **14**, 68–85 (2019).

Acknowledgements

We thank the PPP3CA Hope Foundation (https://www.ppp3ca.org/) for fruitful discussions. We acknowledge initial efforts to analyze the interaction of TAK1 with CN by Dr. Sarah Sheftic and help with the CN:RII crystallization by Dr. Thomas Moon. The authors would like to thank staff

members at the Stanford Synchrotron Radiation Light source (SSRL), SLAC National Accelerator Laboratory for access to X-ray beamlines. Use of the Stanford Synchrotron Radiation Lightsource, SLAC National Accelerator Laboratory, is supported by the U.S. Department of Energy, Office of Science, Office of Basic Energy Sciences under Contract No. DE-AC02-76SF00515. This work was supported by grant R01GM144483 from the National Institute of General Medicine and R01NS124666 from the National Institute of Neurological Disorders and Stroke to WP and grant R01GM098482 from the National Institute of General Medicine to RP. In part, this research was supported by the PPP3CA Hope Foundation Inc (to WP).

Author Contributions

RP and WP developed the concept. KTS, TP and LESFM expressed and purified all proteins. TP and LESFM performed NMR experiments. LESFM and KTS performed ITC experiments. KTS crystallized CN_{D90A}:*tp*TAK1 and determined the structures of the CN_{D90A}:*tp*TAK1 and CN:RII complexes. TP crystalized and determined the structure of CN_{E282K}:NHE1. HTN, GP and ANK performed phospho-library and phosphoproteomics experiments. HTN, TP and ANK analyzed MS data. MLD interpreted CN activity data. RP, KTS, TP and WP wrote the manuscript with comments and inputs from all co-authors.

Competing Interests Statement

The authors declare no competing interests. The funders had no role in study design, data collection and analysis, decision to publish, or preparation of the manuscript.

Table 1. *pTAK1* dephosphorylation by CN wildtype vs variants at [0.5 μM]

	Δ% for TAK1 dephosphorylation between CN_{WT} and CN variants	
CN variant	Δ%	P value
CN_{wt}	100% ± 8	n/a
CN_{E237K}	51% ± 4	< 0.0001
CN_{E282K}	31% ± 2	< 0.0001
$CN_{E237K/E282K}$	47% ± 3	< 0.0001
CN_{Q284K}	192% ± 7	< 0.0001
CN_{D285K}	159% ± 7	< 0.0001
CN_{Y315A}	162% ± 6	< 0.0001

All experiments were performed as experimental replicates n=6; mean ± s.d.; unpaired T-test with two-sided P value (threshold 0.05).

Table 2. Comparing activity of RII_{WT} vs RII_{V98R}

	Δ% for RII_{WT} vs RII_{V98R}			
CN variant	RII_{WT}	P value	RII_{V98R}	P value
CN_{wt}	100 ± 4	n/a	143 ± 4	< 0.0001
CN_{E237K}	48 ± 2	< 0.0001	28 ± 1	< 0.0001
CN_{E282K}	35 ± 2	< 0.0001	16 ± 1	< 0.0001

All experiments were performed as experimental replicates n=6; mean ± s.d.; unpaired T-test with two-sided P value (threshold 0.05)

Figure Legends

Figure 1. **TAK1 binds to CN.** (**a**) Domain structure of CN and TAK1, with key constructs used for studies indicated. TAK1 S439 is underlined. The location of the E282, the most frequently observed missense variant in developmental and epileptic encephalopathy (DEE91) is indicated by a pink star. (**b**) ITC thermogram of $TAK1_{384\text{-}474}$ and CN_{WT}. (**c**) Schematic of NMR experiment; ^{15}N-labeled $TAK1_{384\text{-}474}$ alone (dark blue, reference) and with CN (orange). (**d**) 2D [^{1}H,^{15}N] HSQC spectrum of ^{15}N-labeled $TAK1_{384\text{-}474}$ (dark blue) and in complex with CN (orange). (**e**) Plot of peak intensity versus $TAK1_{384\text{-}474}$ sequence for spectra in (d)**.** Motifs of interest indicated above highlighted with grey bars. (**f**) ITC thermogram of $TAK1_{384\text{-}474}$ $LxVP_{dead}$ and CN_{WT}. (**g**) ITC thermogram of $TAK1_{384\text{-}474}$ RRR_{dead} (AAA) and CN_{WT}.

Figure 2. **Substrate-trapped CN_{D90A}:*tp*TAK1 complex**. (**a**) Cartoon illustrating the formation of the CN_{D90A}:*tp*TAK1 complex. (**b**) Crystal structure of the CN_{D90A}:*tp*TAK1 complex. TAK1 (dark blue) binds the CN LxVP binding pocket (pale green surface) which is at the intersection of CN subunits CNA (light gray) and CNB (dark gray). The TAK1 RRR motif binds a pocket adjacent to the CN active site (light yellow; Fe^{2+} shown as sphere). (**c**) Overlay of the LxVP motifs from TAK1 (this study [PDBID 9NXF [https://doi.org/10.2210/pdb9NXF/pdb]]; blue), RII (this study [PDBID: 9NXN [https://doi.org/10.2210/pdb9NXN/pdb]]; red), NHE1 (PDBID: 6NUC [https://doi.org/10.2210/pdb6NUC/pdb], beige) and NFATc1 (PDBID: 5SVE [https://doi.org/10.2210/pdb5SVE/pdb], green). (**d**) TAK1 RRR motif binds a negatively charged pocket adjacent to the active site, with the R_{i-1} residue (cyan) binding a deeply negatively charged pocket defined by CN E282; the E282 binding pocket (yellow dotted line). (**e**) Same view as (d), with the CN surface shown in white and the ionic/polar (dashed black/grey lines, respectively) interactions between TAK1 (blue/cyan sticks) and CN (white sticks) shown. E282 binding pocket shown in pink. (**f**) Substrate (TAK1-*pS*439, phosphorylated with PKA) dephosphorylation assays

with CN variants (colors correspond to label colors in (e)). Data are mean values ± SD; n = 6 technical replicates; ****unpaired T-test with two-sided P value (threshold 0.05), p-value <0.0001.

Figure 3. **The dephosphorylation of canonical CN substrate RII is enhanced with an i-1 arginine**. (**a**) Domain structure of RIIα, with WT and V98R (making it an R_{i-1} containing substrate) constructs shown (PKA phosphorylates S99). LxVP sequences shown. (**b**) RII substrate (phosphorylated on S99 by PKA) dephosphorylation assays with WT (solid boxes) and V98R (dashed boxes) vs different CN variants (as indicated). Data are mean values ± SD; n = 6 technical replicates; **** unpaired T-test with two-sided P value (threshold 0.05), p-value <0.0001.

Figure 4. **The PPP3CA DEE91 E282K variant (CN_{E282K}) alters the recruitment of R_{i-1}-containing substrates to CN**. (**a**) The most frequently identified nucleotide missense mutation in PPP3CA-related DEE91 patients. (**b**) Superposition of the crystal structures of CN_{E282K} (pink; PDBID 9NXE [https://doi.org/10.2210/pdb9NXE/pdb] [this study]) and CN_{WT} (grey; PDBID 6NUC [https://doi.org/10.2210/pdb6NUC/pdb]) bound to NHE1. Bound NHE1 residues shown as sticks and beige surface. E282K (pink) and E282 (grey) shown as sticks and boxed. (**c**) Same overlay as shown in (b), illustrating the ionic interactions between E282K and E237 in CN_{E282K}. (**d-f**) Overlay of CN_{E282K} (E282K; bound to NHE1) and CN_{D90A} (E282; bound to TAK1), with the E282K/E237 and E282/E237 residues shown as sticks with either the CN_{D90A} (d) or the CN_{E282K} (e,f) electrostatic surface potential. Ionic interactions between E282K and E237 shown as black dashed lines (e,f); overlaid TAK1 RRR motif residues displayed as sticks (f). (**g**) TAK1-pS439 variants dephosphorylation assays (phosphorylated with PKA) with CN_{wt} or CN_{E282K}. Data are mean values ± SD; n = 3 technical replicates; ****unpaired T-test with two-sided P value (threshold 0.05), p-value <0.0001.

Figure 5. **The PPP3CA-related DEE91 CN missense mutation E282K globally alters CN substrate dephosphorylation.** (**a**) Schematic of in vitro peptide array dephosphorylation assay (Created in BioRender. Parikh, T. (2026) https://BioRender.com/4abz3wd). (**b**) Peptide array dephosphorylation data analysis. (**c**) CN_{WT} (left) preferentially dephosphorylates X-X-R-pS/T and X-X-K-pS/T peptides while CN_{E282K} (pink) preferentially dephosphorylates X-X-D/E-pS/T peptides. (**d**) Phosphosite preference motif for CN_{WT} (upper) and CN_{E282K} (lower, pink shade) based on peptides identified in the fast cluster of the in vitro dephosphorylation assay.

Figure 6. **The effect of the CN missense mutation E282K in N2A cells.** (**a**) IP-MS of CN_{wt} in N2A cells with the most enriched and known CN interactors highlighted; significance assessed by two-sided Student's T-test. (**b**) Comparison between IP-MS of CN_{wt} and CN_{E282K} in N2A cells highlighting which known CN regulators are enriched (blue) or depleted (pink) in CN_{E282K} ; significance assessed by two-sided Student's T-test. (**c**) Phosphoproteomics data from CN_{WT} and CN_{E282K} expressing N2A cells; significance assessed by two-sided Student's T-test. (**d**) Phosphosite preference motif for sites dephosphorylated by CN_{Wt} (top) compared to sites dephosphorylated by CN_{E282K} (bottom) in CN_{WT} and CN_{E282K} expressing N2A cells.

Editorial Summary

De novo Calcineurin (CN) variants cause DEE91, with E282K being the most common. E282K alters CN's acidic substrate binding pocket to basic, thus shifting substrate preference and dephosphorylation signaling, subsequently impacting neurodevelopment.

Peer review information: *Nature Communications* thanks the anonymous reviewers for their contribution to the peer review of this work. A peer review file is available.

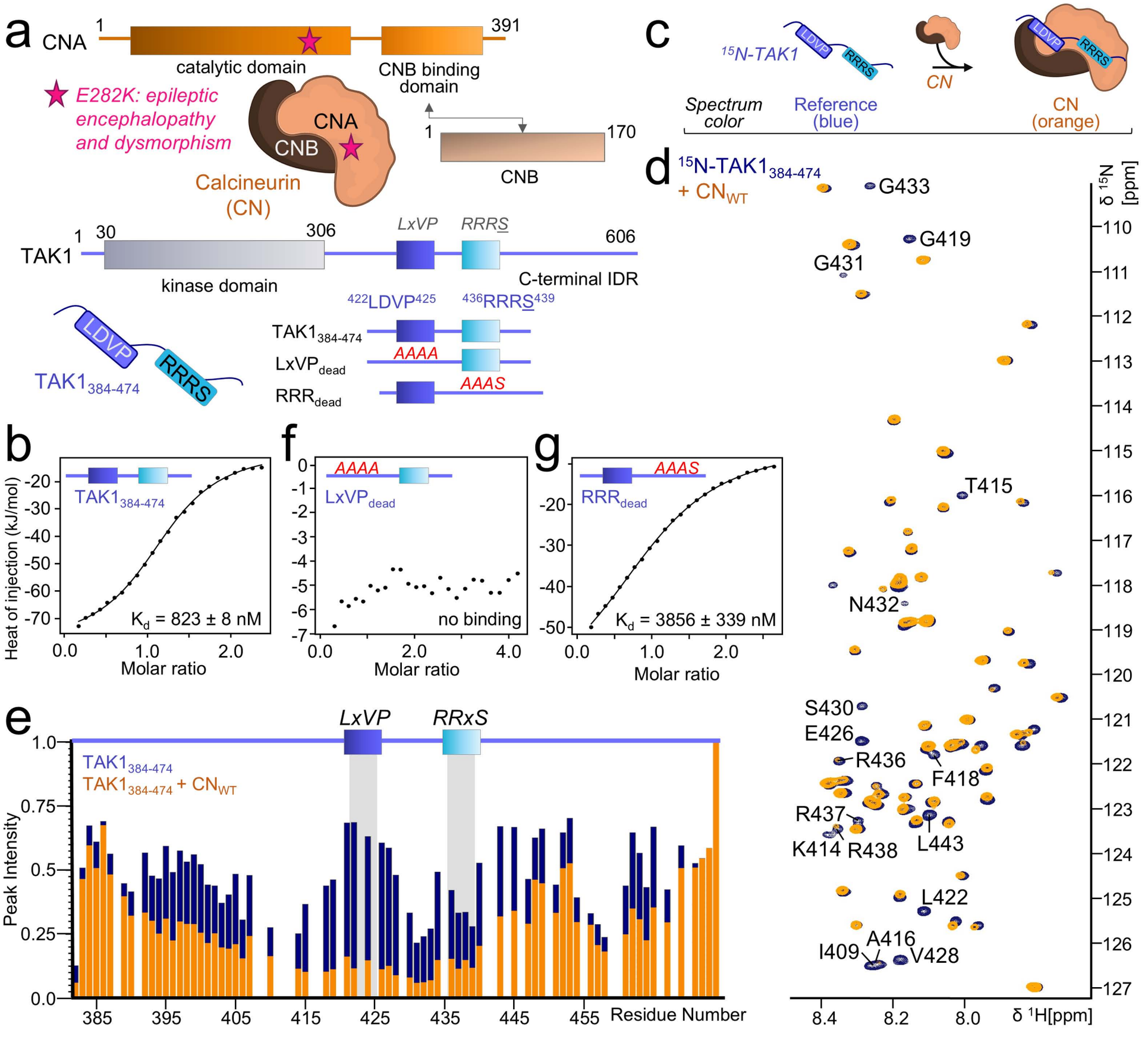
a
CNA
1
391
catalytic domain
CNB binding domain
E282K: epileptic encephalopathy and dysmorphism
CNA
CNB
Calcineurin (CN)
1
170
CNB
TAK1
1
30
306
LxVP
RRRS
606
kinase domain
C-terminal IDR
422LDVP425
436RRRS439
LDVP
RRRS
TAK1384-474
TAK1384-474
AAAA
LxVPdead
AAAS
RRRdead
c
15N-TAK1
LDVP
RRRS
CN
Spectrum color
Reference (blue)
CN (orange)
d
15N-TAK1384-474 + CNWT
G433
G419
G431
T415
N432
S430
E426
R436
F418
R437
K414
R438
L443
L422
A416
I409
V428
δ 15N [ppm]
δ 1H[ppm]
b
TAK1384-474
Heat of injection (kJ/mol)
Kd = 823 ± 8 nM
Molar ratio
f
AAAA
LxVPdead
no binding
Molar ratio
g
AAAS
RRRdead
Kd = 3856 ± 339 nM
Molar ratio
e
LxVP
RRxS
TAK1384-474
TAK1384-474 + CNWT
Peak Intensity
Residue Number

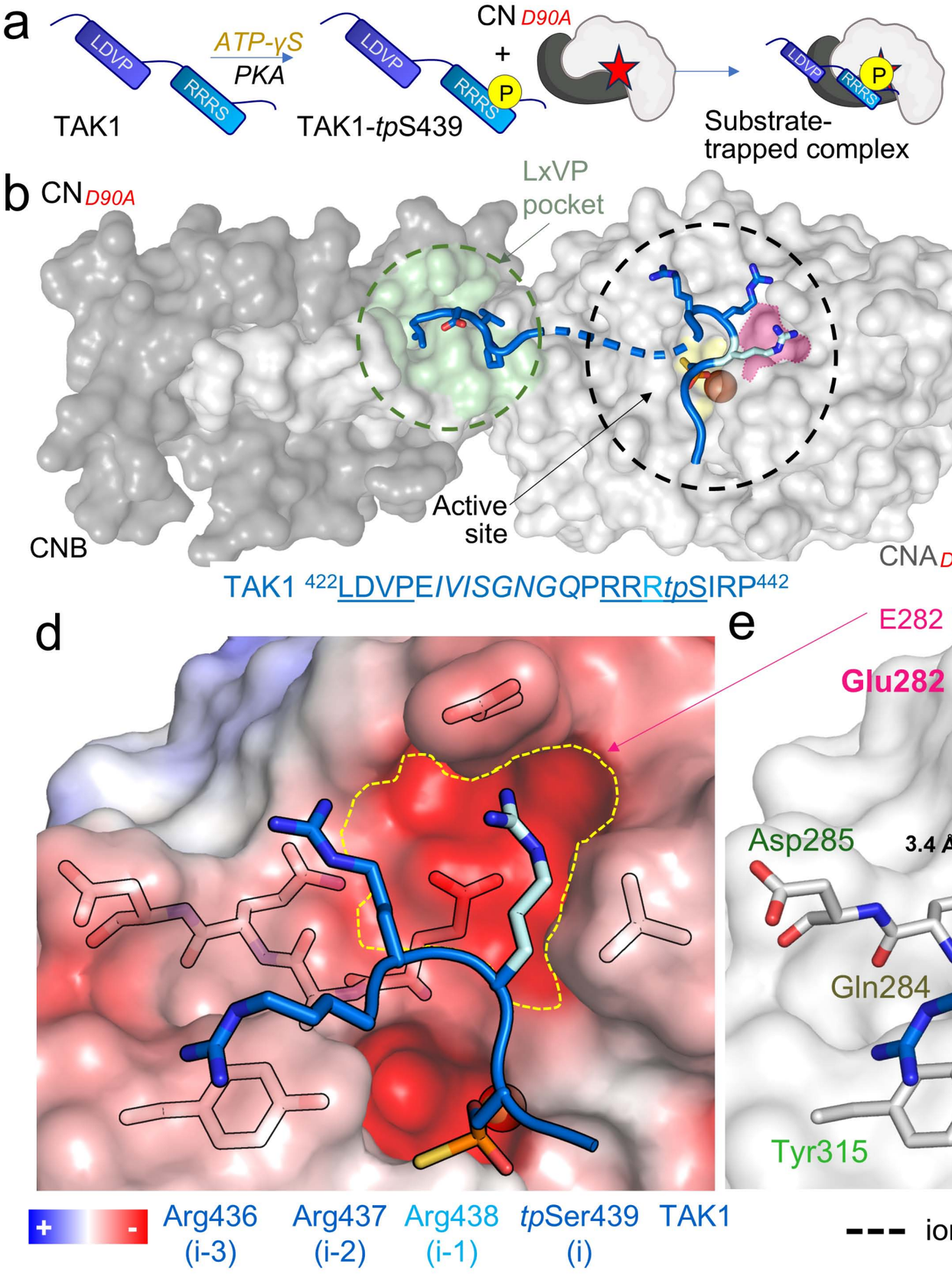
a
LDVP
RRRS
TAK1
ATP-γS
PKA
TAK1-tpS439
P
CN D90A
+
Substrate-
trapped complex
b CN D90A
LxVP
pocket
Active
site
CNB
CNA D90A
TAK1 422LDVPEIVISGNGQPRRRtpSIRP442

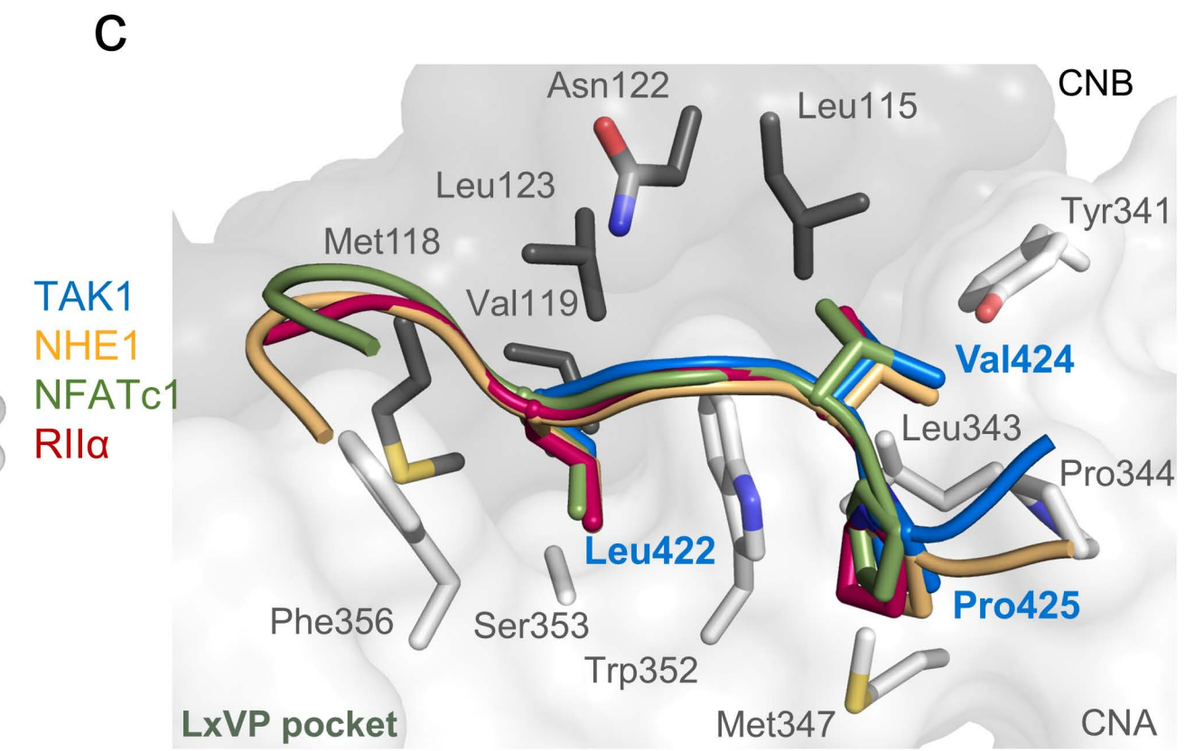
c
TAK1
NHE1
NFATc1
RIIα
CNB
Asn122
Leu115
Leu123
Tyr341
Met118
Val119
Val424
Leu343
Pro344
Leu422
Pro425
Phe356
Ser353
Trp352
Met347
LxVP pocket
CNA

d
Arg436
(i-3)
Arg437
(i-2)
Arg438
(i-1)
tpSer439
(i)
TAK1

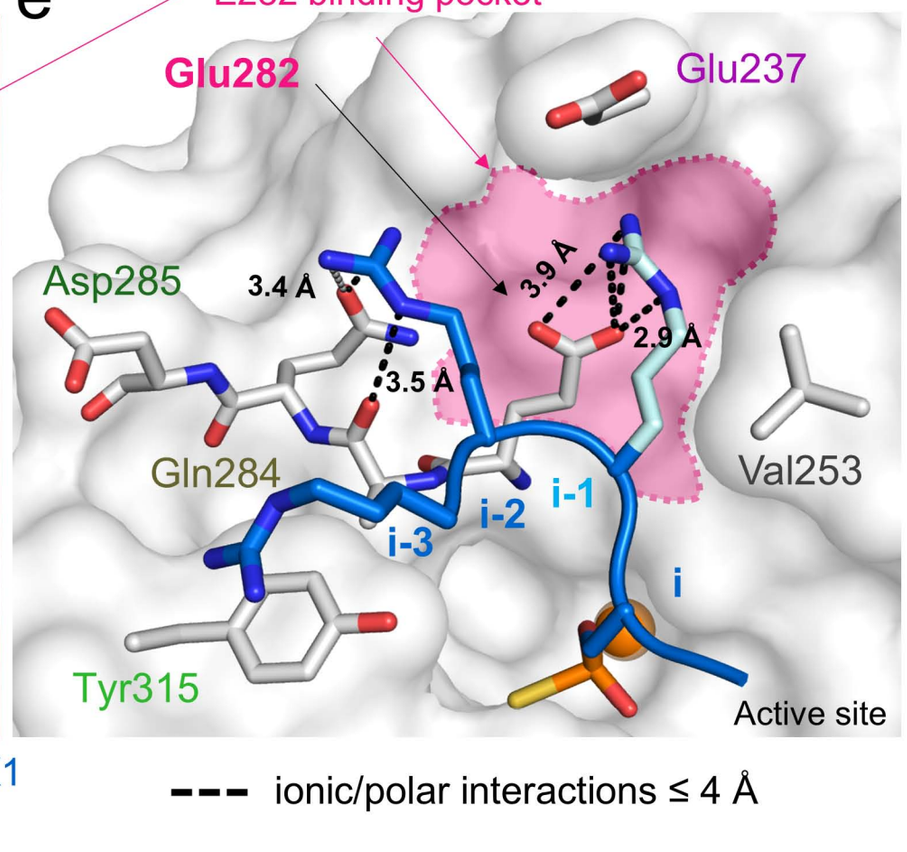
e
E282 binding pocket
Glu282
Glu237
Asp285
3.4 Å
3.5 Å
3.9 Å
2.9 Å
Gln284
Val253
i-3
i-2
i-1
i
Tyr315
Active site
--- ionic/polar interactions ≤ 4 Å

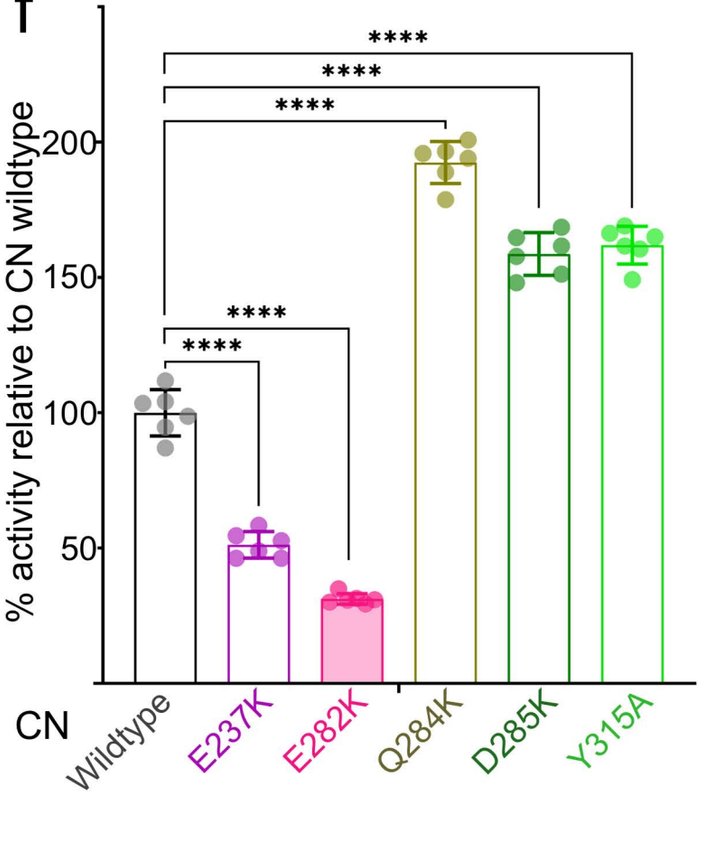
f
% activity relative to CN wildtype
200
150
100
50
****
****
****
****
****
CN
Wildtype
E237K
E282K
Q284K
D285K
Y315A

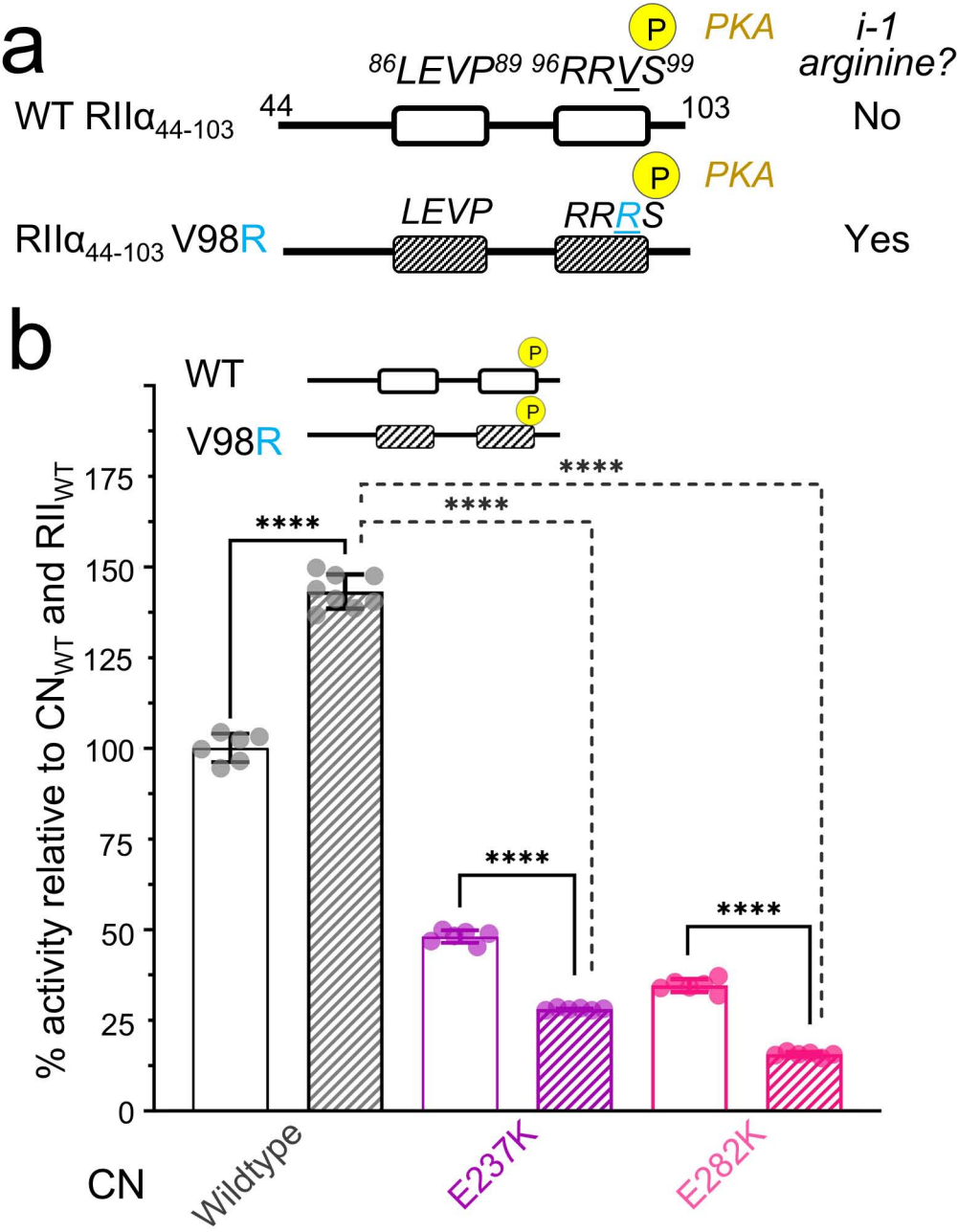
a
P
PKA
i-1 arginine?
86LEVP89 96RRVS99
WT RIIα44-103
44
103
No
P
PKA
LEVP
RRRS
RIIα44-103 V98R
Yes
b
WT
V98R
P
P
% activity relative to CNWT and RIIWT
175
150
125
100
75
50
25
0
****
****
****
****
****
CN
Wildtype
E237K
E282K

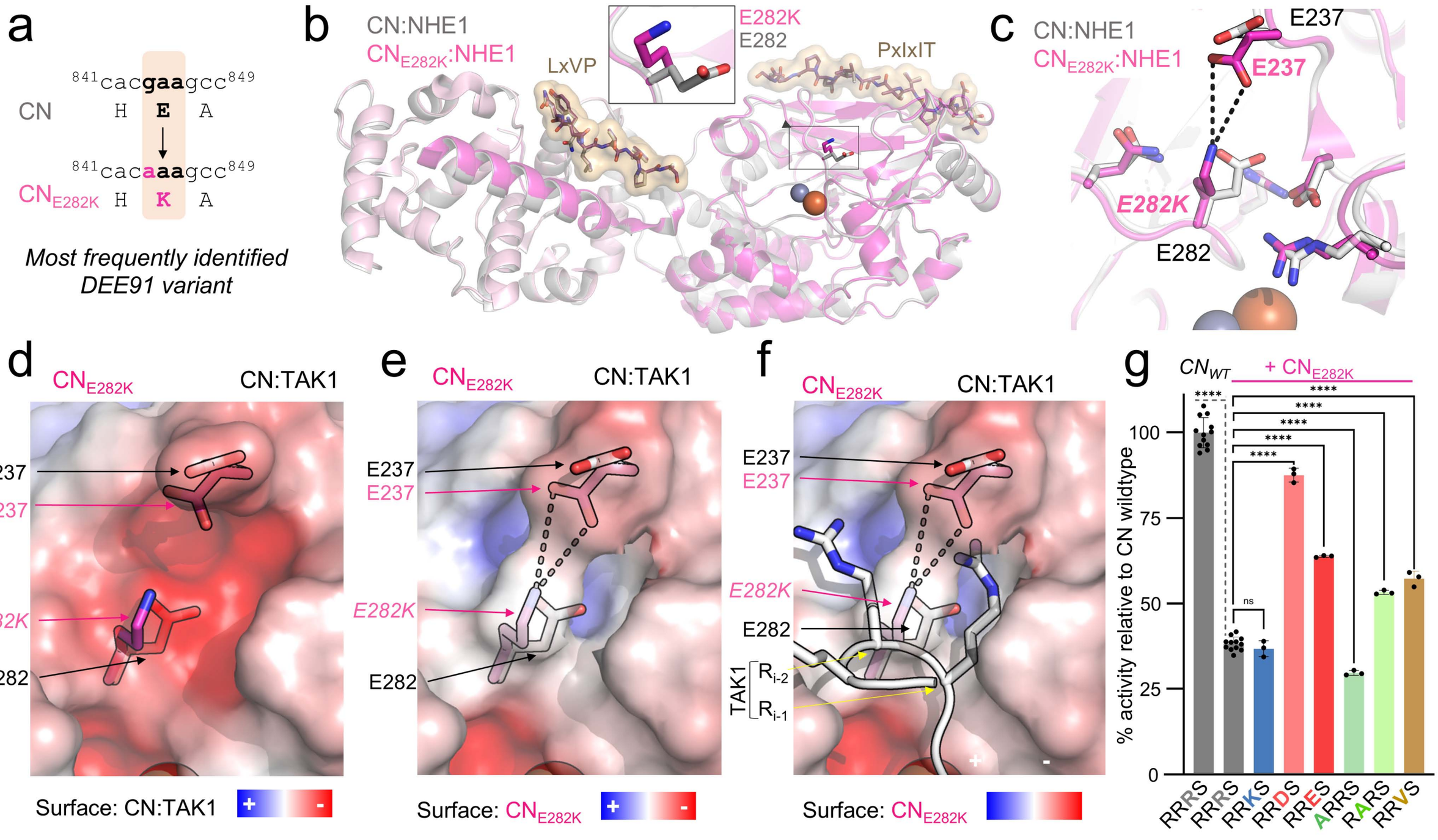
a
841cacgaagcc849
CN H E A
841cacaaagcc849
CNE282K H K A
Most frequently identified DEE91 variant
b
CN:NHE1
CNE282K:NHE1
LxVP
E282K
E282
PxIxIT
c
CN:NHE1
CNE282K:NHE1
E237
E237
E282K
E282
d
CNE282K
CN:TAK1
E237
E237
E282K
E282
Surface: CN:TAK1
+
-
e
CNE282K
CN:TAK1
E237
E237
E282K
E282
Surface: CNE282K
+
-
f
CNE282K
CN:TAK1
E237
E237
E282K
E282
TAK1
Ri-2
Ri-1
+
-
Surface: CNE282K
g
CNWT
+ CNE282K
% activity relative to CN wildtype
100
75
50
25
0
****
ns
RRRS
RRRS
RRKS
RRDS
RRES
ARRS
RARS
RRVS

a

Timescale *in vitro* peptide array dephosphorylation assay

Dephosphorylation

TMT- phosphopeptide library

control

+ CN_{WT} and CN_{E282K}

quench 0 15 30 60 120

minute

Quantitative Phosphoproteomics

combine

LC-MS

Relative abundance

m/z

motif analysis

All *p-sites*

↓

single, localized *p-sites*

↓

significantly correlated and present in 2/3 replicates

↓

motif generation

b

	CN_{WT}	CN_{E282K}
# substrate peptides (total)	1274	1267

substrate motif	#	#
X – X – R –*pS/T*	51	42
X – X – K –*pS/T*	29	26
X – X –D/E –*pS/T*	171	172

i-3 i-2 i-1 i

aa position relative to phosphosite i

Phospho-ser/thr peptides dephosphorylated by CN

↓

sort phospho-peptides by sequence motif

↓

compare phosphosite motif and dephosphorylation rate

c

Phosphosite Motif

CN_{WT}

# of peptide substrates

X-X-X-R-pS/T — 51

X-X-X-K-pS/T — 29

X-X-X-D/E-pS/T — 171

0 20 40 60 80 100 %

CN_{E282K}

# of peptide substrates

42

26

172

0 20 40 60 80 100 %

slow fast

slow → fast

Phosphopeptide Dephosphorylation Rate

d

CN_{WT} - in vitro fast

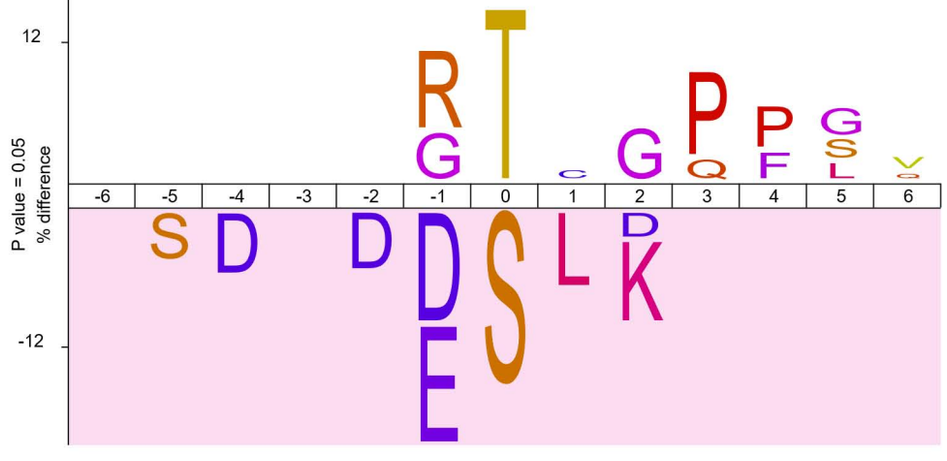

CN_{E282K} - in vitro fast

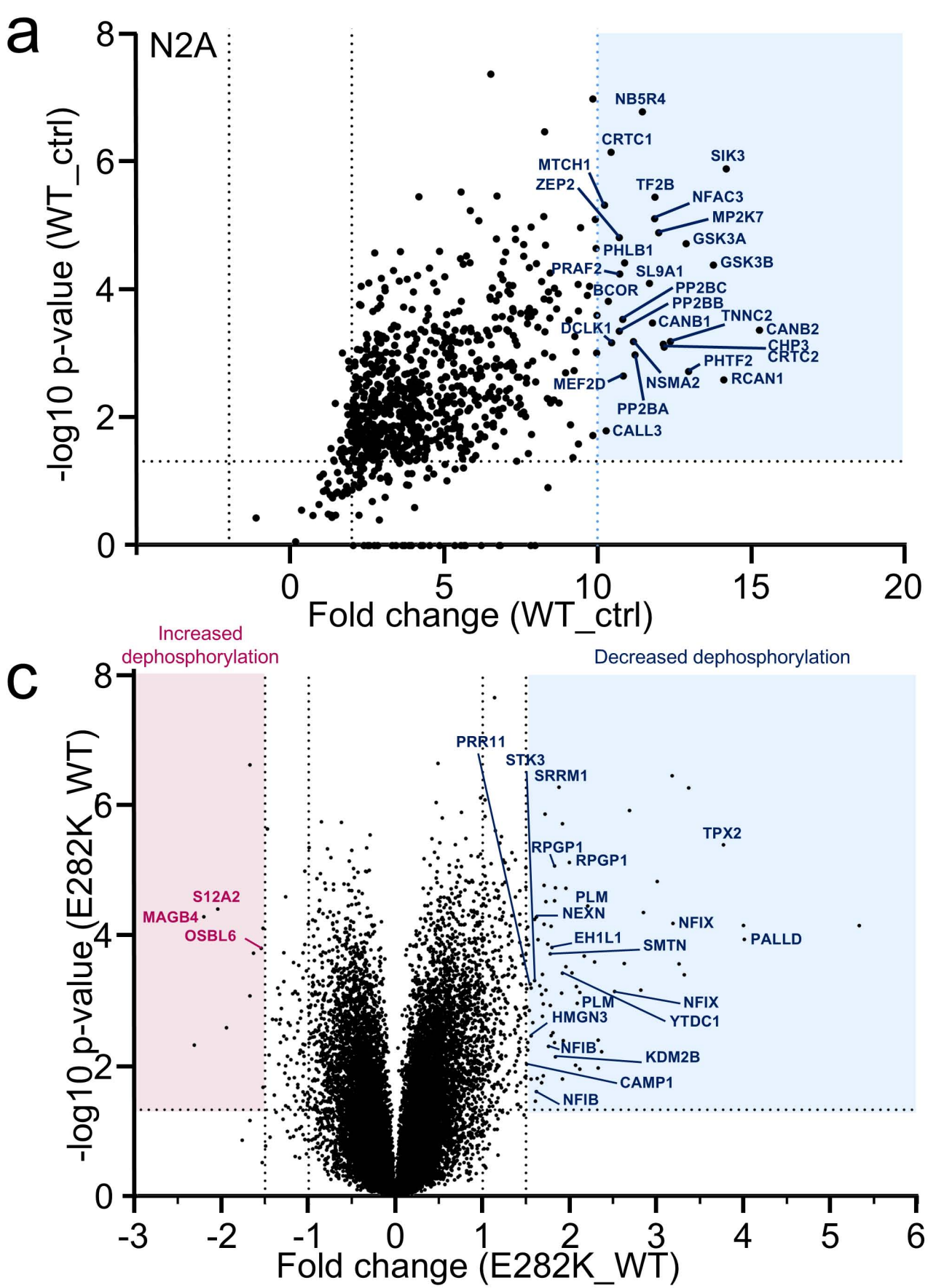
a
N2A
-log10 p-value (WT_ctrl)
Fold change (WT_ctrl)
NB5R4
CRTC1
SIK3
MTCH1
ZEP2
TF2B
NFAC3
MP2K7
GSK3A
PHLB1
GSK3B
PRAF2
SL9A1
BCOR
PP2BC
PP2BB
CANB1
TNNC2
CANB2
DCLK1
CHP3
CRTC2
PHTF2
MEF2D
NSMA2
RCAN1
PP2BA
CALL3
b
Depleted in CN_E282K
Enriched in CN_E282K
-log10 p-value (E282K_WT)
Fold change (E282K_WT)
SL9A1
MP2K7
PHLB1
NSMA2
PI4KA
TF2B
CHP3
MTCH1
TTC7B
NFAC3
RCAN3
RCAN1
BCOR
c
Increased dephosphorylation
Decreased dephosphorylation
-log10 p-value (E282K_WT)
Fold change (E282K_WT)
PRR11
STK3
SRRM1
TPX2
RPGP1
RPGP1
S12A2
MAGB4
OSBL6
PLM
NEXN
NFIX
EH1L1
SMTN
PALLD
PLM
NFIX
HMGN3
YTDC1
NFIB
KDM2B
CAMP1
NFIB
d
N2A
CN_WT
CN_E282K
P value = 0.05
% difference